BRNO UNIVERSITY OF TECHNOLOGY
VYSOKÉ UČENÍ TECHNICKÉ V BRNĚ

FACULTY OF MECHANICAL ENGINEERING
FAKULTA STROJNÍHO INŽENÝRSTVÍ

INSTITUTE OF MATHEMATICS
ÚSTAV MATEMATIKY

NEW APPROACHES IN AIRBORNE THERMAL IMAGE PROCESSING FOR LANDSCAPE ASSESSMENT
NOVÉ PŘÍSTUPY ZPRACOVÁNÍ LETECKÝCH OBRAZOVÝCH TERMÁLNÍCH DAT K HODNOCENÍ KRAJINY

DOCTORAL THESIS
DIZERTAČNÍ PRÁCE

AUTHOR — Ing. Marek Pivovarník
AUTOR PRÁCE

SUPERVISOR — doc. Ing. Mgr. František Zemek, Ph.D.
ŠKOLITEL

BRNO 2016

Abstrakt
Letecká termální hyperspektrální data přinášejí řadu informací o teplotě a emisivitě zemského povrchu. Při odhadování těchto parametrů z dálkového snímání tepelného záření je třeba řešit nedourčený systém rovnic. Bylo navrhnuto několik přístupů jak tento problém vyřešit, přičemž nejrozšířenější je algoritmus označovaný jako Temperature and Emissivity Separation (TES). Tato práce má dva hlavní cíle: 1) zlepšení algoritmu TES a 2) jeho implementaci do procesingového řetězce pro zpracování obrazových dat získaných senzorem TASI. Zlepšení algoritmu TES je možné dosáhnout nahrazením používaného modulu normalizování emisivity (tzv. Normalized Emissivity Module) částí, která je založena na vyhlazení spektrálních charakteristik nasnímané radiance. Nový modul je pak označen jako Optimized Smoothing for Temperature Emissivity Separation (OSTES). Algoritmus OSTES je připojen k procesingovému řetězci pro zpracování obrazových dat ze senzoru TASI. Testování na simulovaných datech ukázalo, že použití algoritmu OSTES vede k přesnějším odhadům teploty a emisivity. OSTES byl dále testován na datech získaných ze senzorů ASTER a TASI. V těchto případech však není možné pozorovat výrazné zlepšení z důvodu nedokonalých atmosférických korekcí. Nicméně hodnoty emisivity získané algoritmem OSTES vykazují více homogenní vlastnosti než hodnoty ze standardního produktu senzoru ASTER.

Abstract
Airborne thermal hyperspectral data delivers valuable information about the temperature and emissivity of the Earth's surface. However, attempting to derive temperature and emissivity from remotely sensed thermal radiation results in an underdetermined system of equations. Several approaches have been suggested to overcome this problem, but the most widespread one is called the Temperature and Emissivity Separation (TES) algorithm. This work focuses on two major topics: 1) improving the TES algorithm and 2) implementing it in a processing chain of image data acquired from the TASI sensor. The improvement of the TES algorithm is achieved by replacing the Normalized Emissivity Module with a new module, which is based on smoothing of spectral radiance signatures. The improved TES algorithm is called Optimized Smoothing for Temperature Emissivity Separation (OSTES). The OSTES algorithm is appended to a pre-processing chain of image data acquired from the TASI sensor. The testing of OSTES with simulated data shows that OSTES produces more accurate and precise temperature and emissivity retrievals. OSTES was further applied on ASTER standard products and on TASI image data. In both cases is not possible to observe significant improvement of the OSTES algorithm due to imperfect atmospheric corrections. However, the OSTES emissivitites are smoother than emissivities delivered as ASTER standard product over homogeneous surfaces.

klíčové slova
dálkový průzkum Země, letecké obrazové data, termální hypespektrální data, separace teploty a emisivity, TASI senzor, algoritmus, tepelné záření

key words
remote sensing, airborne image data, thermal hyperspectral data, temperature and emissivity separation, TASI sensor, algorithm, thermal infrared

PIVOVARNÍK, M. New Approaches in Airborne Thermal Image Processing for Landscape Assessment. Brno: Vysoké učení technické v Brně, Fakulta strojního inženýrství, 2017. 63 s. Vedoucí dizertační práce doc. Ing. Mgr. František Zemek, Ph.D.

I declare that I have written the doctoral thesis *New Approaches in Airborne Thermal Image Processing for Landscape Assessment* on my own according to advice of my supervisor doc. Mgr. Ing. František Zemek, Ph.D., and using the sources listed in references.

November 25, 2016 Ing. Marek Pivovarník

I would like to express my gratitude to my supervisor František Zemek for supervising my Ph.D. thesis, for his wise opinions and for his trust in my decisions.

I would also like to express my gratitude to Siri Jodha Singh Khalsa and Juan Carlos Jiménez-Muñoz for advising me. I really appreciate their attitude to help whenever I needed it.

I would like to thank my colleagues Jan Hanuš and Lucie Homolová for helpful consultations and inspirational comments to my work.

Finally, I would like to thank Daniela for her support and patience during my studies.

Ing. Marek Pivovarník

Contents

Introduction

Remote sensing refers to acquisition of information without making physical contact. The term, as used nowadays, is mostly used in the context of data acquired from airborne and satellite platforms. Acquired information is electromagnetic (EM) radiation emitted or reflected from the Earth. It is a powerful tool for observing the land surface, atmosphere and oceans, which results in many applications in different fields including meteorology, ecology, global change studies, agriculture, sociology, urban studies and many others [71].

Remote sensing activities can be divided into the groups according to the different regions of EM spectrum which is used. The boundaries between EM regions are not sharply defined. According to the [77], the EM spectrum can be divided into visible (0.4 – 0.72 µm), near infrared (0.72 – 1.3 µm), short-wave infrared (1.3 – 3 µm), mid-wave infrared (3 – 8 µm), long-wave infrared (8 – 14 µm) and microwave (1 mm – 1 m) region. In the first three mentioned regions EM radiation can be observed which is mainly reflected from the Earth's surface. The EM radiation in long-wave infrared region, also widely referred as the *thermal* infrared (TIR) region, consists mainly of the radiation emitted by the Earth's surface. Mid-wave infrared consists of mixture of reflected and emitted EM radiation. Microwave radiation is sensed by radar systems for active remote sensing. Data acquisition is also limited by atmosphere transmittance, which can be very weak between individual regions.

The sensors used for acquisition of EM radiation are categorised into broadband, multispectral and hyperspectral. Broadband sensors are continuously sensitive within the one region of EM spectrum while multispectral sensors consist of few, rather wide, spectral bands within one region of EM spectrum. Hyperspectral sensors are similar to multispectral, but acquire data in many very narrow and consecutive spectral bands.

The first airborne thermal multispectral sensor was developed in 1980 by NASA Jet Propulsion Laboratory. This sensor consisted of five multispectral bands in the thermal region. Currently operational airborne sensors are Airborne Hyperspectral Scanner (AHS) and Spatially Enhanced Broad Array Spectrograph System (SEBASS). To our best knowledge, there are currently three commercially available airborne thermal hyperspectral sensors, namely Thermal Airborne Spectrographic Imager (TASI) (Itres Ltd., Calgary, Canada), AISA Owl (Specim Ltd., Oulu, Finland) and Hyper-Cam LW (Telops Inc., Quebec, Canada).

Regarding the the various types of remote sensing data, the focus of this work will be put on processing of image data obtained from multispectral and hyperspectral sensors in the TIR region (i.e. the data are obtained by a sensor acquiring emitted EM radiation in the region of 8 – 14 µm in several spectral bands). This work primarily focuses on processing of airborne thermal hyperspectral data acquired by the TASI sensor, however, other sensor types will be mentioned as well.

Airborne thermal hyperspectral data offer valuable information about the observed objects. Image data of this kind has found application in fields focused on evapotranspiration [49], vegetation [52], soil moisture [58], mineral mapping [47], urban studies [63] and gas plumes identification [51]. Let us emphasize that the most important quantities derived form airborne thermal hyperspectral data are temperature and emissivity. However, direct derivation of temperature and emissivity by observing radiance in N bands

results in N equations but $N+1$ unknowns (N emissivities plus temperature). This problem, separating the contributions of temperature and emissivity to observed radiances, has been the subject of a great deal of research and many methods have been developed to address it [44].

The most widely used spaceborne sensor with multispectral TIR capabilities is the Advanced Spaceborne Thermal Emission and Reflection Radiometer (ASTER). It is part of the NASA's Terra platform, which was launched in December 1999. The temperature and emissivity separation algorithm [25], designated TES, that was developed for the ASTER sensor has since been applied to processing of TIR image data acquired by various airborne and spaceborne, and various multispectral and hyperspectral sensors.

Although the TES algorithm is already capable of producing reasonably accurate results it could be made more robust, precise and widely applicable by reducing the number of the assumptions that it makes. In particular, for surfaces with low spectral contrast TES often produces anomalous emissivity spectra [17, 59]. These spectra suffer from a large degree of noise, which can be explained by the use of various thresholds included in TES.

The aims of this work are: 1) enhancing the accuracy and precision of the products generated by the TES algorithm and 2) incorporating a new algorithm to the processing chain applied on image data acquired by TASI sensor. The chapters discussing the aims of the work are preceded by Chapter 1 and Chapter 2, which introduce fundamental laws of thermal radiation and basic principles of the processing of airborne thermal hyperspectral data. Chapter 2 describes in detail all pre-processing steps applied to image data acquired by the TASI sensor necessary for initiation of the temperature and emissivity separation procedure. These steps create a pre-processing chain, which will be followed by the temperature and emissivity separation procedure.

Chapter 3 describes the problem of temperature and emissivity separation and introduces currently used algorithms with emphasis on the TES algorithm. This chapter also introduces the improvement of the TES algorithm, which is referred to as Optimized Smoothing for Temperature and Emissivity Separation (OSTES). The main improvement is accomplished by replacing one of the TES modules with a newly designed one that takes advantage of a relationship between brightness temperature and emissivity.

The results of the OSTES performance testing are described in the Chapter 4. The OSTES algorithm is firstly tested on a set of simulated data representing different natural materials as they would be acquired by various multispectral and hyperspectral sensors. Then it is applied on the ASTER standard land-leaving and downwelling radiance product AST_09T and the results are compared with the ASTER emissivity and surface kinetic temperature standard products AST_08 and AST_05, respectively. Last part of this chapter includes incorporation of the OSTES algorithm to the processing chain of image data acquired by the TASI sensor and then it compares the performance of the OSTES and TES algorithms on image data obtained from TASI.

1

Theoretical background on thermal radiation

This chapter describes fundamental principles and concepts of EM radiation called *thermal radiation*. Every object with temperature above 0 K emits thermal radiation. The amount of thermal radiation as a function of wavelength depends on the object's temperature and its surface properties.

Black body

The concept of black body is very well described in the work of Howell [32], where black body is defined as perfect absorber for all incident radiation. In addition to being a perfect absorber, the black body is perfect emitter as well. Thus a black body absorbs and reemits all energy incident upon it. Black body do not exist in nature but the concept is used for determination of a real object's surface property called emissivity.

Planck's law

Concerning black body at thermal equilibrium, the amount and spectral distribution of emitted energy is described by Planck's law [50]:

$$B(T,\lambda) = \frac{2hc^2}{\lambda^5}\frac{1}{e^{\frac{hc}{\lambda kT}} - 1},$$

where $B(T,\lambda)$ is spectral radiance ($\mathrm{W\,m^{-2}\,\mu m^{-1}\,sr^{-1}}$) of black body at temperature T (K) and wavelength λ (µm); k is Boltzmann constant ($1.3806488 \cdot 10^{-23}\,\mathrm{J\,K^{-1}}$), h is Planck constant ($6.62606957 \cdot 10^{-34}\,\mathrm{J\,s}$) and c is speed of light ($299792458\,\mathrm{m\,s^{-1}}$). An example of the black body radiation at three different temperatures, as described by Planck's law, is depicted in Figure 1.1a.

Emissivity

Emissivity is defined as the ratio of radiance of a real surface to that of a black body at the same temperature:

$$\varepsilon(T,\lambda) = \frac{L(T,\lambda)}{B(T,\lambda)},$$

where $\varepsilon(T,\lambda)$ is spectral emissivity and $L(T,\lambda)$ is real surface spectral radiance. The emissivity can be understood as real surface emission effectiveness in comparison with

radiation emitted by a black body of the same temperature in the same wavelength. Let us note that emissivity depends on the viewing angle apart from temperature and wavelength, as is defined in Hollow [32]. In remote sensing observed objects are of the temperature between 270 – 330 K and the observation angle is close to nadir (usually maximum off-nadir angle is less than 30°), which causes negligible changes in spectral emissivity of most of natural surfaces. Thus, it can be further assumed that emissivity depends just on wavelength.

Quartz was chosen to demonstrate the principles of radiation of a real object's surfaces. Its spectral emissivity was taken from the ASTER spectral library [6] and it is shown in Figure 1.1b. Quartz heated to the temperature T has spectral radiance $L(T, \lambda) = \varepsilon(\lambda)B(T, \lambda)$ as is illustrated in Figure 1.1c.

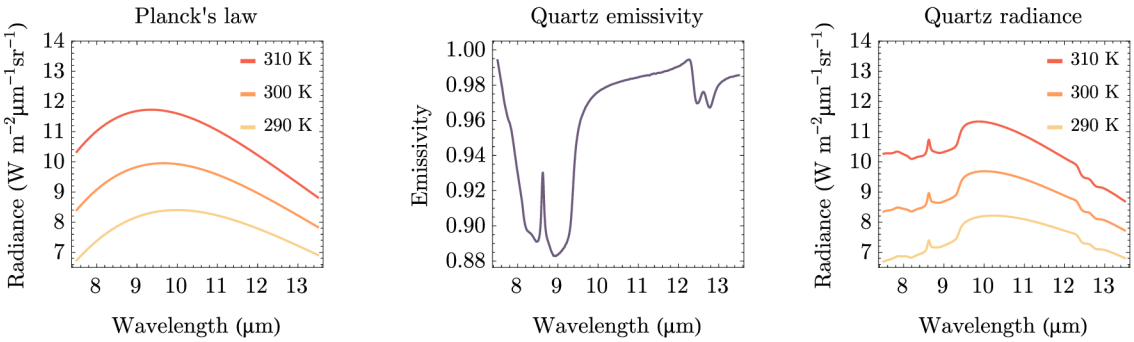

(a) Radiation of black body described by Planck's law

(b) Quartz spectral emissivity

(c) Radiance of quartz

Figure 1.1: Principles of radiation of real surfaces.

Wien's displacement law

The peak of black body radiation at wavelength λ_{max} is described by Wien's displacement law [32]:

$$\lambda_{max} = \frac{b}{T},$$

where b is Wien's displacement constant (2.8977721×10^{-3} m K). As was mentioned before, the temperature of most of natural and artificial surfaces observed by airborne remote sensing ranges in 270 – 330 K. According to the Wien's displacement law, the peak of emitted radiation varies roughly from 8.8 µm to 10.7 µm. This range is in coincidence with the atmospheric window situated between 8 µm to 13 µm. The atmospheric transmittance in this atmospheric window is very high and thus it is relevant for acquisition of remotely sensed thermal data.

Kirchhoff's law of thermal radiation

Emitting and absorbing properties of an object at local thermodynamic equilibrium surrounded by an isothermal environment are related through by Kirchhoff's law of thermal

radiation [42]. It states that an object's surface absorptivity $\alpha(\lambda)$ at a given wavelength is equal to the object's surface emissivity $\varepsilon(\lambda)$ at the same wavelength:

$$\alpha(\lambda) = \varepsilon(\lambda).$$

Energy conservation implies that energy incident to the object's surface can be reflected, transmitted or absorbed. Considering the fractions of incident energy the following equation holds:

$$1 = \rho(\lambda) + \tau(\lambda) + \alpha(\lambda),$$

where $\rho(\lambda)$ is the object's surface spectral reflectivity, $\tau(\lambda)$ is the object's surface spectral transmissivity and $\alpha(\lambda)$ is the object's surface spectral absorptivity. Applying Kirchhoff's law to opaque material ($\tau(\lambda) = 0$) results in following equation:

$$1 = \rho(\lambda) + \varepsilon(\lambda) \quad \Rightarrow \quad \rho(\lambda) = 1 - \varepsilon(\lambda). \tag{1.1}$$

All mentioned principles in this section will be further used in explanation of properties of airborne thermal hyperspectral data and its processing.

2

Airborne thermal hyperspectral data properties

This chapter provides insights into technical parameters of the TASI and processing chain of image data acquired by this sensor. Knowledge of the instrument parameters and processing chain gives important overview of the image data properties and their components. The result of the processing chain described in this chapter is a georeferenced image data containing land-leaving radiance. Such an image data form an input for further processing. Let us note that this chapter omits naming physical quantities dependent on wavelength as "spectral" for the sake of clarity. However, all quantities remain wavelength dependent.

2.1. Instrument technical specifications

The TASI sensor is developed by Itres Ltd. (Calgary, Canada) and is one of the very few commercially available pushbroom hyperspectral TIR sensors equipped with a mercury cadmium telluride array. Each of its 600 across-track imaging pixels contains 32 bands all of which are in the TIR region. Bands are situated in the 8 to 11.5 µm region and have a Full Width at Half Maximum FWHM ≈ 0.11 µm with Noise Equivalent Temperature difference NEΔT ≈ 0.1 K. The response functions of the TASI sensor are described by the Gaussian functions as depicted in Figure 2.1a.

The shape of the response functions implies that any quantity observed by TASI sensor is of finite spectral-bandwidth. Quantities need to be transformed to band-effective quantities in order to relate them with certain wavelengths. The band-effective quantities are obtained by using the weighted average:

$$X_i = \frac{\int_{\lambda_1}^{\lambda_2} r_i(\lambda) X(\lambda)\,\mathrm{d}\lambda}{\int_{\lambda_1}^{\lambda_2} r_i(\lambda)\,\mathrm{d}\lambda}, \tag{2.1}$$

where $r_i(\lambda)$ is the response function of band i, λ_1 and λ_2 are the lower and upper boundaries of band i and X can be substituted by any quantity. Figure 2.1b illustrate the radiance of quartz (solid line) and band-effective values of radiance measured by the TASI sensor (red dots). A sensor of this type is available at the Global Change Research Institute CAS (Brno, Czech Republic) and it is a part of the Flying Laboratory of Imaging Systems (FLIS) [28].

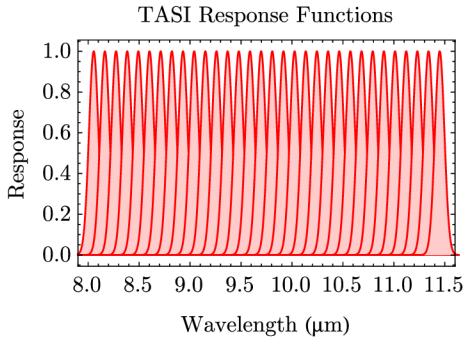

(a) Response functions of TASI sensor.

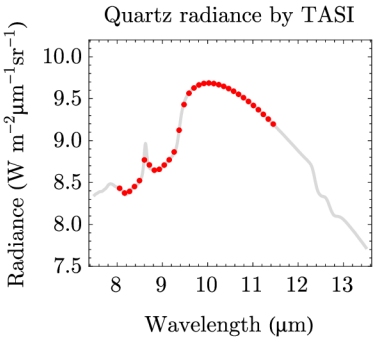

(b) Radiance of quartz at 300 K measured by TASI sensor

Figure 2.1: TASI response functions.

2.2. Image data pre-processing

The main objective of image data pre-processing is transformation of acquired raw image data into georeferenced radiance at surface level. It is accomplished by three major steps: radiometric calibration, atmospheric corrections and geometric pre-processing. Radiometric calibration converts digital numbers (DN) into values of radiance at sensor level. Atmospheric corrections compensates the influence of the intervening atmosphere and produces land-leaving radiance. Finally, the geometric pre-processing compensates for image data distortions caused by aircraft movement and registers the image data into a coordinate system.

Supportive field measurements of thermal radiance, surface temperature, emissivity and atmospheric parameters offers valuable data for calibration and validation purposes. Especially in cases of airborne image data for scientific purposes the high quality is strongly demanding. Thus it is necessary to perform supportive measurements in order to achieve precise results and determine the data quality.

It is important to emphasize that currently there does not exist any definitive standard pre-processing chain. This is caused mainly by a small number of sensors with various technical parameters and their different applications. Sensors usually have tailored pre-processing chains, which is the case of TASI sensor as well. Certain parts of processing chain are maintained by commercial tools. However, there are still parts of processing chain that need to be done by in-house tools. In Figure 2.2 is illustrated the processing chain used at the Global Change Research Institute CAS (Brno, Czech Republic) to pre-process image data acquired by TASI sensor. Individual parts of the diagram will be discussed in the following text. The radiometric calibration and atmospheric corrections are demonstrated with an example of quartz radiance at 300 K as depicted in Figure 2.3.

Radiometric calibration

Thermal radiation incident upon the sensor array originates from many additive components (e.g. observed scene, instrument enclosure, intervening atmosphere and others). Incident thermal radiation produces an electrical signal, which is proportional to radiant intensity. This electrical signal is then amplified and converted into voltage and subse-

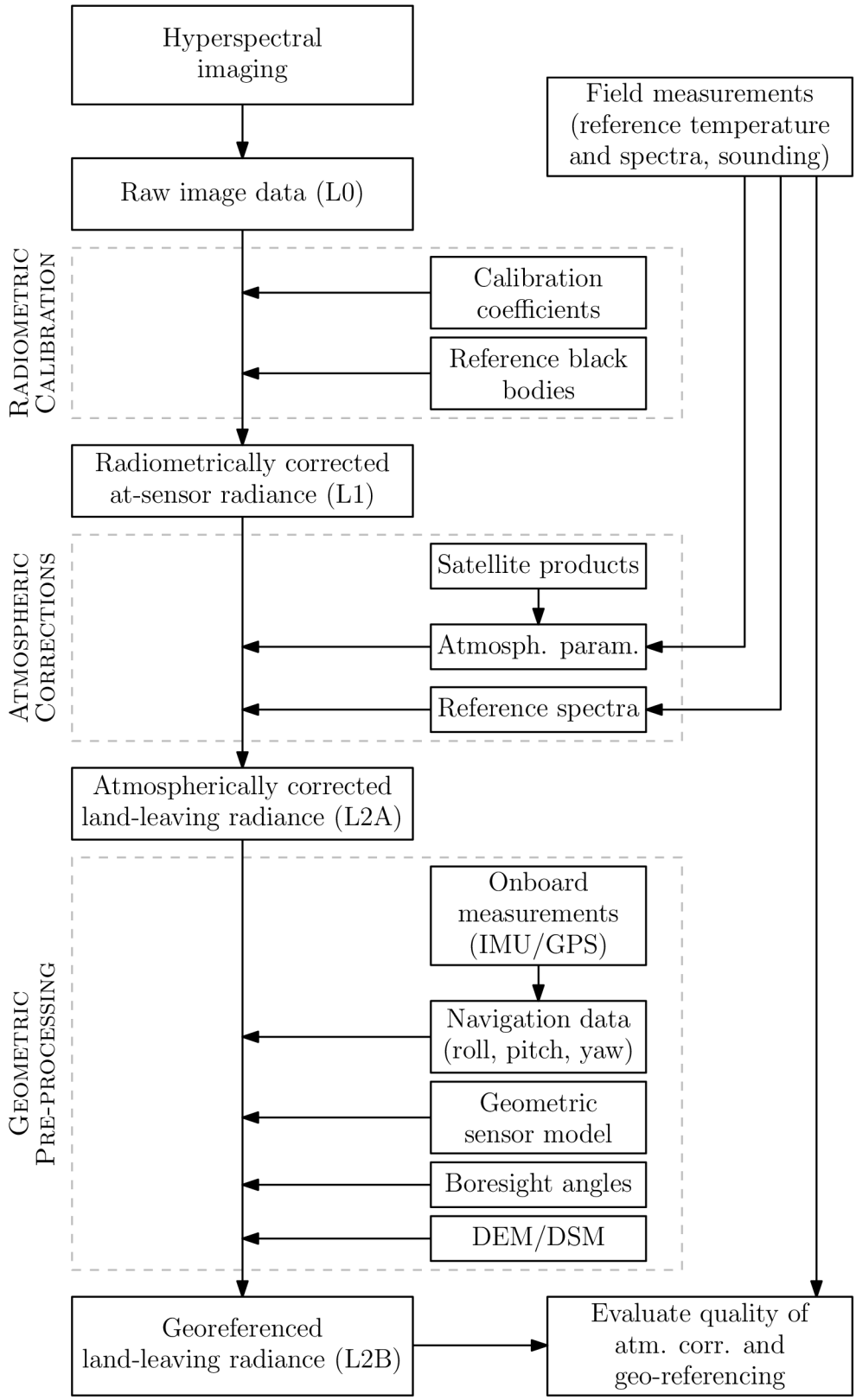

Figure 2.2: Processing chain applied to image data acquired by TASI sensor.

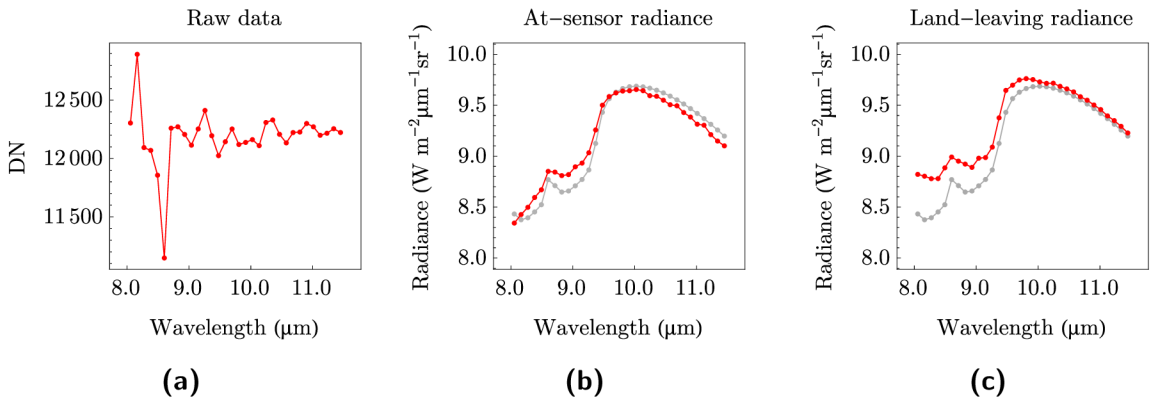

Figure 2.3: Example of data at various processing stages. Data simulates quartz at 300 K as would be acquired by TASI sensor at altitude of 2000 m under summer mid-latitude atmosphere: (a) shows raw data, (b) shows data after radiometric calibration (in red) and (c) shows data after corrections of atmospheric transmissivity and upwelling atmospheric radiance (in red). In cases (b) and (c) pure quartz radiance are shown in gray.

quently into DN values (as depicted in Figure 2.3a). Radiometric calibration consists of separating signal from the viewed scene and converting it into physical units of radiance. Atmosphere influence is not accounted in this process and thus after radiometric calibration one gets radiance at sensor level (as depicted in Figure 2.3b).

The relationship between DN and at-sensor radiance L_{m} is the following:

$$\mathrm{DN} = a + bL_{\mathrm{m}},$$

where a and b are calibration coefficients. The calibration coefficient a, also known as offset, represents radiation originating from instrument enclosure, sensor dark current and electronic offset. The calibration coefficient b, also called gain, determines sensor radiant sensitivity. Calibration coefficients are determined by imaging a set of reference black bodies of known temperature and emissivity. In this context, the term black body is meant to be a surface with emissivity very close to unity. These coefficients are usually determined applying one of two methods: 1) imaging two black bodies at different temperature directly before imaging, or 2) combining black body image data from laboratory and black body image data acquired before imaging.

In the first case are usually used two black bodies of different temperatures. Temperatures of these black bodies enclose temperatures expected to occur in the scene. Let us consider the radiance of cold black body $L(T_{\mathrm{C}})$ and the radiance of hot blackbody $L(T_{\mathrm{H}})$. The calibration coefficients can be obtained from:

$$\begin{aligned} a &= \frac{\mathrm{DN_H}L(T_{\mathrm{C}}) - \mathrm{DN_C}L(T_{\mathrm{H}})}{L(T_{\mathrm{C}}) - L(T_{\mathrm{H}})} \\ b &= \frac{\mathrm{DN_C} - \mathrm{DN_H}}{L(T_{\mathrm{C}}) - L(T_{\mathrm{H}})}, \end{aligned}$$

where $\mathrm{DN_C}$ and $\mathrm{DN_H}$ are digital numbers measured by sensor viewing cold black body and hot black body, respectively. This procedure is commonly used in case of other instruments for measuring thermal radiation, such as μFTIR [30].

The determination of calibration coefficients in the second case assumes that gain calibration coefficient b does not change under different conditions. Thus, it is sufficient to perform series of black body measurements at different temperatures in order to determine gain calibration coefficient b. These measurements can be performed in the laboratory once per season. However, offset calibration coefficient a does not remain stable and changes under different conditions. Hence, it is necessary to image a black body at known temperature directly before acquisition to account for variability of this coefficient.

Again, it is important to emphasize that all quantities and both calibration coefficients are wavelength dependent. Spectral calibrations are part of the radiometric calibrations. To determine spectral calibrations, band centers of every pixel using laser beam at different wavelengths are determined in the laboratory. Determined positions do not change over time significantly. However, the spectral shift occurs under different conditions and thus it needs to be determined for every scene. Spectral shift estimation is usually based on the spectral features of the atmosphere or certain materials.

In case of TASI sensor, commercial software for radiometric calibration delivered by Itres company (Calgary, Canada) is used. SparCal software [35] is used to determine all parameters necessary for radiometric calibrations from laboratory measurements. RCX software [36] is used for additional estimation of calibration parameters and for processing raw image data. The resulting radiometrically calibrated image data are radiance at sensor level L_{m}.

Atmospheric corrections

Radiometric calibrations deliver image data containing radiation from the surface, attenuated by atmosphere, plus radiation from the atmosphere along the line of sight. Thus the measured radiance at sensor level (L_{m}) consists mainly of radiance emitted from the land surface, downwelling atmospheric radiance ($L^{\downarrow}_{\mathrm{atm}}$) reflected by the surface and the atmospheric upwelling radiance ($L^{\uparrow}_{\mathrm{atm}}$). The sum of all these components is expressed by a radiative transfer equation (RTE) as follows:

$$L_{\mathrm{m}} = \tau\varepsilon B(T_{\mathrm{s}}) + \tau(1-\varepsilon)L^{\downarrow}_{\mathrm{atm}} + L^{\uparrow}_{\mathrm{atm}}, \tag{2.2}$$

where $B(T_{\mathrm{s}})$ is radiance of the surface at temperature T_{s} according to the Planck's law, ε is the surface's emissivity and τ is atmospheric transmittance. It is important to emphasize that all elements in the equation are wavelength dependent but notation for this is omitted for the sake of clarity. Since sensors are of finite bandwidth, quantities in eq. (2.2) are replaced by band-effective equivalents according to the eq. (2.1). Moreover, RTE can be used under the assumption of cloud-free atmosphere under local thermodynamic equilibrium. The meaning of the RTE is illustrated in the Figure 2.4, where ρ is reflectivity. Kirchhoff's law of thermal radiation implies that reflectivity ρ can be rewritten as $(1-\varepsilon)$ for opaque materials, as shown in eq. (1.1).

The goal of the atmospheric corrections is to determine atmospheric transmittance, downwelling and upwelling atmospheric radiance and compensate for them. The quantification of these quantities is usually based on radiative transfer models of the atmosphere. For this purpose MODerate resolution atmospheric TRANsmission (MODTRAN) model [8] is usually used. MODTRAN simulates atmospheric parameters such as atmospheric transmittance, downwelling and upwelling atmospheric radiance based on input parameters such as vertical profiles of water vapour content and temperature, CO_2 concentration,

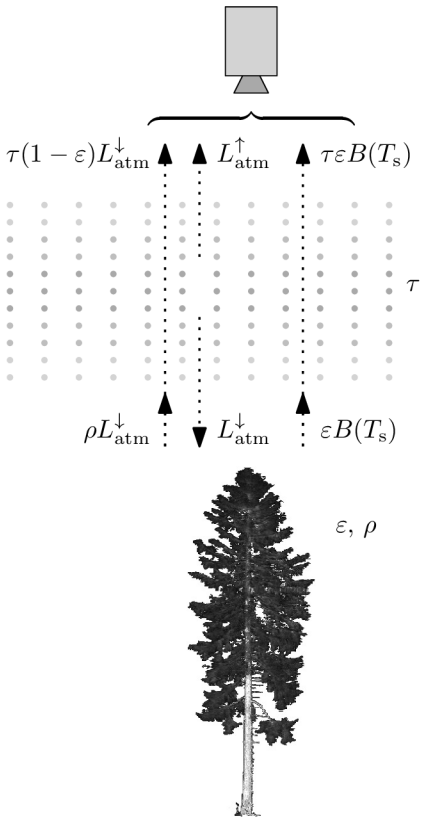

Figure 2.4: The radiance incident to the sensor in the thermal region originates mainly from three sources: 1) radiance $\tau\varepsilon B(T_s)$ emitted by an object; 2) reflected downwelling atmospheric radiance $\tau(1-\varepsilon)L^{\downarrow}_{\mathrm{atm}}$; 3) upwelling atmospheric radiance $L^{\uparrow}_{atm}$ emitted by the atmosphere itself.

the choice of model atmosphere (if measured profiles are not available) and many others. In general, input parameters can be obtained in two ways: 1) by *in-situ* measurements; 2) by satellite-based products.

The most common *in-situ* measurement is radio sounding. A radiosonde is launched during the overflight and it is used to measure vertical temperature and water vapour profile of the atmosphere. Other *in-situ* instruments can be used as well, for example sunphotometer for obtaining water vapor content or different radiometers for measuring sky or surface radiance. Another source of water vapour and temperature profiles is satellite-based products acquired close to the time of aircraft overflight. The most common is MOD07_L2 product [9] generated by Moderate Resolution Imaging Spectroradiometer (MODIS) instrument. Illustration of the transmittance, downwelling and upwelling atmospheric radiance generated by MODTRAN using MOD07_L2 products as input are depicted in Figure 2.5.

In case of thermal hyperspectral images, various algorithms for estimating atmospheric effects based just on the image data itself were developed. Usually it is applied to one of the following: In-Scene Atmospheric Corrections (ISAC) introduced by Young et al. [76] and Autonomous Atmospheric Compensation (AAC) introduced by Gu et al. [26]. The advantage of using one of these algorithms is that no supporting data are necessary. The drawback of these methods remains in estimation of just atmospheric transmittance and upwelling atmospheric radiance.

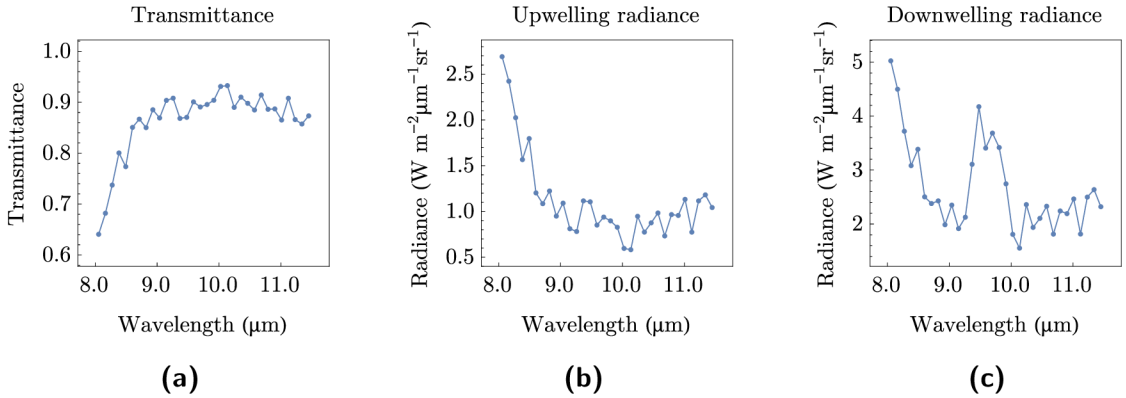

Figure 2.5: Example of atmospheric parameters used for atmospheric correction of TASI image data acquired at altitude of 2000 m above surface during summer season.

Once all the atmospheric parameters are determined, it remains to compensate for them. Compensating for atmospheric transmittance and upwelling atmospheric radiance leads to land-leaving radiance (L_{LL}):

$$L_{\mathrm{LL}} = \varepsilon B(T_{\mathrm{s}}) + (1-\varepsilon)L^{\downarrow}_{\mathrm{atm}}. \tag{2.3}$$

The example of land-leaving radiance is shown in Figure 2.3c. The contribution fro downwelling atmospheric radiance is not possible to separate without knowledge of emissivity. Hence, image data after atmospheric corrections are made of land-leaving radiance L_{LL}. Compensation for downwelling atmospheric radiance is part of the temperature and emissivity separation described in Chapter 3.

Atmospheric corrections for the TASI sensor, as part of processing chain, are not performed by commercial products. However, there exists commercial tools that allow complex solution for atmospheric corrections. An example of such a tool is ATCOR [53] which is based on look-up tables generated by MODTRAN and takes into account terrain topography and sensor parameters. It offers basic temperature and emissivity separation algorithms as well. Apart from the mentioned solution, atmospheric corrections rely on extracting data from *in-situ* measurements or satellite products, running radiative transfer models and applying derived atmospheric parameter on image data. Alternatively, algorithms for atmospheric parameters estimation from image data can be implemented. In both cases, atmospheric corrections involve creating in-house tools.

Geometric pre-processing

Acquired image data are distorted during their acquisition and geometric pre-processing accounts for all factors causing these distortions. During geometric pre-processing aircraft motion, terrain variations and geometric sensor model are taken into account in order to register image data into reference frame.

Ancillary data about aircraft position and movement, terrain structure and geometric sensor model are necessary. The aircraft needs to be equipped with IMU/GNSS systems for recording aircraft position (longitude, latitude and altitude) and aircraft orientation (roll, pitch and heading angles). Terrain structure is obtained from Digital Surface Model (DSM) or Digital Elevation Model (DEM). These data are derived from aerial laser scanning or from stereo images. Aerial laser scanning can be performed either simultaneously

with image data acquisition or separately. Other sources of DEM/DSM are national services or satellite products (e.g. ASTER product AST14DEM). The geometric sensor model is usually delivered by the sensor manufacturer.

The process applied on image data during geometric pre-processing is called geo-orthoreferencing. It consists of two successive steps: direct image data geocoding and resampling. Direct image data geocoding consists of geometric corrections and orthogonalization of the image data. These are further resampled into a regular grid of the reference frame with the desired coordinate system (e.g. Universal Transverse Mercator coordinate system). Image data are resampled into desired spatial resolution applying nearest neighbor, bilinear or cubic interpolation. For scientific purposes nearest neighbor interpolation is commonly used since it preserves spectral information and does not combine spectra from surrounding pixels.

Geometric pre-processing of image data acquired by TASI sensor are performed by GeoCor software [37] delivered by Itres company (Calgary, Canada). The difference between distorted image data and georeferenced image data is illustrated in Figure 2.6.

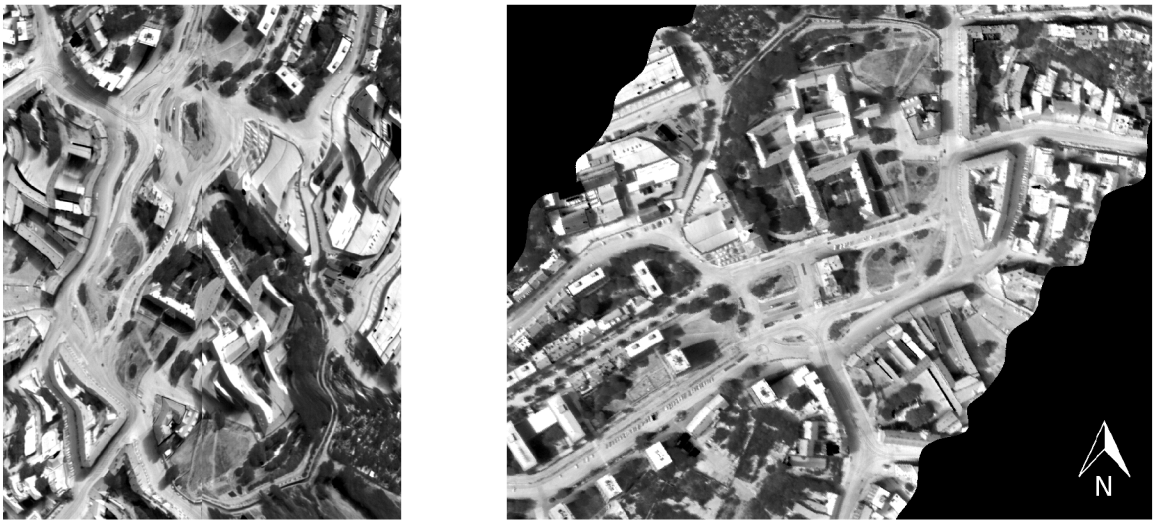

(a) Distorted raw geometry image data.

(b) Georeferenced image data.

Figure 2.6: Illustration of land-leaving radiance image data before and after geometric pre-processing.

3

Temperature and emissivity separation

Pre-processed thermal image data provide valuable information about the properties of the observed surfaces, most importantly their temperature and emissivity. But in order to determine temperature and emissivity from observed radiance one must solve a system of RTEs. Data from multispectral and hyperspectral TIR sensors offer the opportunity to derive both the temperature as well as emissivity spectrum, which can be used to characterize the material composition of surfaces. However, observing radiance in N bands yields N radiative transfer equations but $N + 1$ unknowns (N emissivities plus temperature), which results in the underdetermined system of equations. The estimation of temperature and emissivity from such a system of equations is usually addressed as *temperature-emissivity separation*. This chapter describes several approaches for separating temperature and emissivity. It firstly introduces a few commonly used methods and then focuses on the most popular approach called the Temperature and Emissivity Separation algorithm (TES). The last part of this chapter focuses on enhancing the accuracy and precision of the products generated by the TES algorithm. The main improvement is accomplished by replacing one of the TES modules with a newly designed one that takes advantage of a relationship between brightness temperature (i.e. temperature obtained from land-leaving radiance under the assumption of emissivity $\varepsilon = 1$) and emissivity. The improved TES algorithm is called Optimized Smoothing for Temperature Emissivity Separation (OSTES) and is introduced in [1].

3.1. Available approaches

Many approaches have been developed to overcome the problem of having an underdetermined system of RTEs [44]. Methods used to overcome the problem of underdetermined system of RTEs are usually based on adding empirical or semiempricial constraints.

Algorithms for temperature and emissivity estimation depend on sensor architecture and acquisition context. Some algorithms require knowledge of Normalized Difference Vegetation Index (NDVI) [64], surface type [57] or even emissivity [38]. Others are based on multitemporal [73] or multiangle [65] acquisition. Only a few algorithms can retrieve temperature and emissivity from a single scene without ancillary surface information, whether using multispectral or hyperspectral data. The most common are: the grey body emissivity method [7], the linear emissivity constraint temperature emissivity separation method [74], spectral smoothing [11] and the TES algorithm [25]. Principles of the last four mentioned methods are described in the following text. The most attention is paid to the TES algorithm, as it is the most popular and it is widely applied to many data.

Gray body emissivity method

Barducci and Pippi [7] proposed an algorithm that is based on an assumption of flat spectral emissivity beyond 10 µm. To solve the system of RTEs it is enough to find at least two spectral bands with the same emissivity. This can be achieved in case of airborne thermal hyperspectral data. The drawback of this method is its sensitivity to instrument noise.

Linear emissivity constraint temperature emissivity separation method

As Wang et al. [74] describe, this method is based on the idea of substituting spectral emissivity with a piecewise linear function. The emissivity spectrum is divided into segments, in which spectral emissivities are assumed to be linearly dependent on wavelength. Thus, it is necessary for every segment to estimate gain and offset. It implies that the number of spectral bands has to be equal to, or greater than number of unknowns resulting from segmentation to piecewise linear functions.

Spectral smoothing

The spectral smoothing algorithm, also known as ARTEMISS (Automatic Retrieval of Temperature and EMIssivity using Spectral Smoothness), was reported by Borel at [10] and [11]. The algorithm is based on the assumption that spectra of solids are much more smooth than spectra of gases. Thus by smoothing spectra one removes spectral features introduced by atmosphere and obtains spectral emissivity. Moreover, current implementation described in [11] includes modified ISAC algorithm called ARTISAC, which estimates atmospheric transmissivity for further choice of the correct atmospheric model. Atmospheric models contain so called TUD (atmospheric Transmissivity, Upwelling and Downwelling atmospheric radiance) and are stored in look-up tables (LUT). Then temperature is varied until the spectral emissivity is the smoothest possible, where the smoothness criterion is the standard deviation of measured radiance minus simulated radiance. The spectral smoothness method can be described briefly by following steps:

1. Estimation of atmospheric transmissivity using ARTISAC algorithm
2. Determination of few the closest atmosphere models from TUD-LUT according to the estimated atmospheric transmissivity
3. Use of these atmosphere models as input to spectral smoothness algorithm for a few pixels chosen from the image and the atmosphere model, which results in smoothest emissivity in most of the cases, is chosen as the correct one
4. Use chosen atmosphere model for the whole image and estimate temperature and emissivity by applying the spectral smoothing procedure

3.2. Temperature and emissivity separation algorithm (TES)

The TES algorithm was originally developed for the ASTER sensor [25]. ASTER was launched in December 1999 onboard NASA's Terra platform. TES has since then found widespread use with other multispectral and hyperspectral sensors. Several studies have discussed the implementation of TES with AHS data [61, 39]. Application of TES to data acquired by the TASI sensor is mentioned in a few studies as well [75, 49]. Apart from the mentioned sensors, the TES algorithm has been modified for the Digital Airborne Imaging Spectrometer (DAIS) sensor [60]. Concerning spaceborne sensors, the TES algorithm has also been suggested for the Spinning Enhanced Visible and Infrared Imager (SEVIRI) [40], the MODIS [33] and the Multispectral Thermal Imager (MTI) [46] data processing. Moreover, the TES algorithm is being suggested for the future HyspIRI mission [34].

The TES algorithm is based on a semi-empirical relationship between spectral contrast (i.e. difference between the highest and lowest values in the emissivity spectrum) and the minimum emissivity. The algorithm consists of three modules, namely the Normalization Emissivity Module (NEM) [22], the Ratio module and the Maximum-Minimum Difference (MMD) module [45]. The inputs to the algorithm are land-leaving radiance L_{LL} and downwelling radiance $L^{\downarrow}_{\mathrm{atm}}$. Let us remind the reader that land-leaving radiance is obtained from eq. (2.2) by compensating for atmospheric transmissivity τ and atmospheric upwelling radiance $L^{\uparrow}_{\mathrm{atm}}$:

$$L_{\mathrm{LL}} = \varepsilon B(T_{\mathrm{s}}) + (1-\varepsilon)L^{\downarrow}_{\mathrm{atm}}. \tag{3.1}$$

The NEM module performs an iterative process for estimating temperature and emissivity, and compensating for the downwelling radiance. The output of the NEM module is an initial estimation of temperature and emissivity. Then the ratio module normalizes the emissivities obtained by the NEM module using their arithmetic mean. Thus one obtains the so called β spectrum, which is less sensitive to sensor noise. Finally, the maximum and minimum of the β spectrum are found and their difference (MMD) is used in following semi-empirical relationship:

$$\varepsilon_{\min} = 0.994 - 0.687 \times \mathrm{MMD}^{0.737}. \tag{3.2}$$

Derivation of eq. (3.2) is explained in following paragraph. Ratioing the β spectrum back to an emissivity spectrum with knowledge of minimum emissivity increases the precision of the emissivity spectrum estimates. The band with the highest emissivity is then used for temperature estimation.

The relationship between spectral contrast and minimum emissivity, shown in eq. (3.2), is a regression based on 86 laboratory spectra of rocks, soils, vegetation, snow and water chosen from the ASTER spectral library [6]. This relationship is depicted in the Figure 3.1. It is important to note that eq. (3.2) is tailored for the ASTER sensor. To apply TES to a different sensor, the regression of $\varepsilon_{\min}$ on MMD must be refined by using sensor specific response functions.

After ASTER was launched, [27] and [54] suggested to replace the power regression shown in eq. (3.2) with linear regression. The replacement is connected with modification of the threshold for separating materials with low spectral contrast. The main advantage

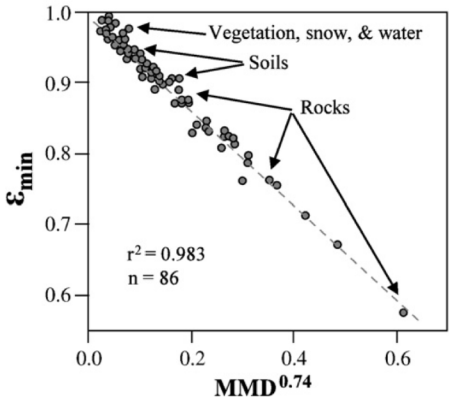

Figure 3.1: Semi-empirical relationship between emissivity contrast and minimum spectral emissivity as shown in study reported by Sabol et al. [54].

is elimination of artefacts in retrievals. However, the drawback is loss of accuracy in cases of materials with low spectral contrast [54]. The TES algorithm used for generation ASTER standard products [5], as well as its modifications for other sensors [61, 39, 75, 60, 40, 33, 46, 34], is based on the power law regression. Thus, in this work the TES algorithm is considered to be that using the power regression.

3.3. TES algorithm improvement

The algorithm described below brings a new approach for separating temperature and emissivity by replacing the NEM module in the TES algorithm with a completely new module. The new module is based on the similarity between brightness temperature spectral features and emissivity spectral features. Brightness temperature is obtained from land-leaving radiance under the assumption of emissivity $\varepsilon = 1$ for every wavelength. Although land-leaving radiance includes some portion of reflected downwelling radiance, it still retains the spectral features arising from the emissivity of the surface materials, which is 0.6 or higher for natural materials [25]. Since the magnitude of downwelling radiance is usually much lower than the surface radiance the features contained in the brightness temperature spectra may be distorted but will not be completely hidden. The new module approximates this relation between brightness temperature T_b and emissivity.

In order to demonstrate the relationship, three emissivity samples with different spectral contrasts were chosen from the ASTER spectral library [6], namely green grass, fine sandy loam and altered volcanic tuff. These emissivities are depicted in Figure 3.2 (solid lines) together with corresponding band-effective values for TASI sensor (empty symbols). These emissivities were applied to Plank's law at temperature 300 K and combined with downwelling radiance from standard mid-latitude summer atmosphere generated by MODTRAN [8]. The resulting radiances, were transformed to band-effective quantities with respect to TASI response functions. Brightness temperatures for every band of each sensor were obtained by applying inverse Planck's law on a sample of land-leaving radiances under the assumption of $\varepsilon = 1$. Figure 3.2 also includes brightness temperatures (full symbols) in order to demonstrate spectral similarity with emissivity. Figure 3.3 plots emissivity against brightness temperature for the chosen samples (empty symbols). These quantities clearly exhibit relationship with linear trend regardless of spectral con-

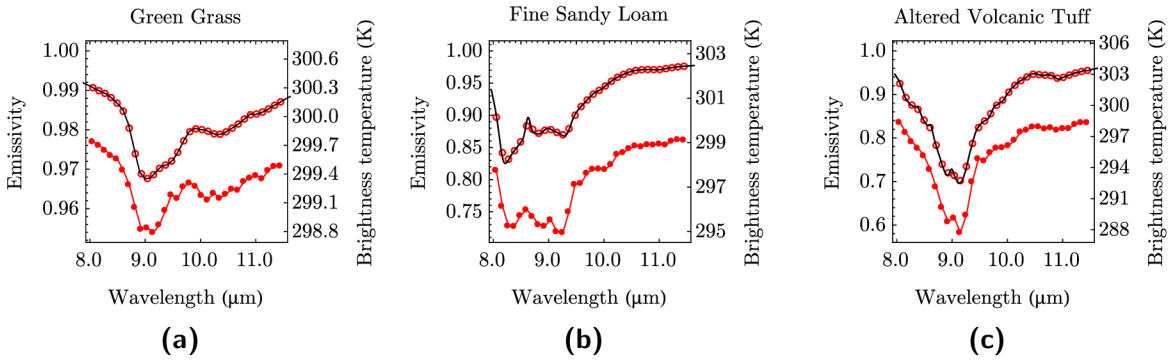

Figure 3.2: Emissivity spectra (black solid line) of three samples chosen from ASTER spectral library [6]. Symbols represent band-effective values of emissivity (empty symbols) and brightness temperature (full symbols) for TASI sensor.

trast. Also displayed in Figure 3.3 are lines that approximate this relationship, derived in the manner described later in the next.

The only factor that can jeopardize the linear relationship between brightness temperature and emissivity is the high magnitude of downwelling radiance in comparison with surface radiance. This will occur rarely, if at all, as described in the first paragraph of this section. Let us emphasise that the brightness temperature and emissivity relationship can be approximated by the linear relationship at any surface temperature since we are interested in the brightness temperature features rather than in absolute values. The algorithm description below uses band-effective values of quantities linked to i-th band by subscript index i.

The dependence of emissivity ε_i on brightness temperature T_{b_i} will be approximated by following equation:

$$\varepsilon_i = pT_{\mathrm{b}_i} + q, \tag{3.3}$$

where p and q are empirical coefficients. These coefficients are determined by solving the system of two equations using two points, namely maximum brightness temperature coupled with emissivity equal to 1 and minimum brightness temperature coupled with lowest emissivity $\varepsilon_{\min}$:

$$\begin{aligned} 1 &= p\max(T_{\mathrm{b}_i}) + q, \\ \varepsilon_{\min} &= p\min(T_{\mathrm{b}_i}) + q. \end{aligned} \tag{3.4}$$

The next step is estimation of the the lowest emissivity $\varepsilon_{\min}$.

This is done by varying $\varepsilon_{\min}$ over the range of possible emissivities for natural materials $[0.6, 1]$, determining corresponding coefficients p and q by solving eq. (3.4) and then approximating emissivity by eq. (3.3) using brightness temperature for all spectral bands. The estimated emissivity is then used together with land-leaving radiance L_{LL} and downwelling radiance $L^{\downarrow}$ (subscript $_{\mathrm{ATM}}$ is omitted for clarity reasons) in a computation that yields spectral radiance:

$$L'_i = \frac{L_{\mathrm{LL}_i} - (1-\varepsilon_i)L_i^{\downarrow}}{\varepsilon_i}. \tag{3.5}$$

The temperature in every spectral band is derived from spectral radiance L' applying inverse Plank's law. The highest one is chosen as the reference temperature $T_{\max}$. Finally,

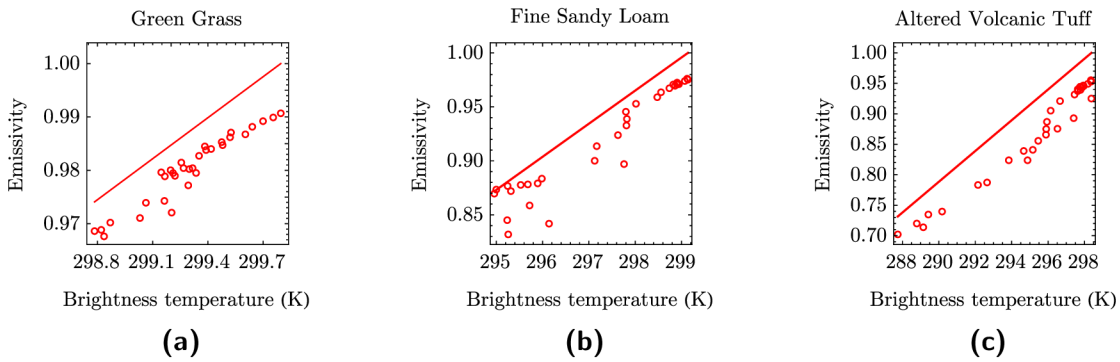

Figure 3.3: Symbols represent examples of the relationship between brightness temperature T_b and emissivity as would be observed by the TASI sensor. Lines illustrate the approximations of the relationship between brightness temperature and emissivity. The procedure used for estimation of the brightness temperature and emissivity relationship is described in the text.

the estimated spectral radiance L' and Planck's law at the reference temperature T_max are normalized and compared against each other as follows:

$$\sum_i \left| \frac{B_i(T_\mathrm{max})}{||B(T_\mathrm{max})||_1} - \frac{L'_i}{||L'||_1} \right| .$$

The value of ε_min is considered final if its corresponding spectral radiance L' is the best fit to Plank's law.

The whole process of determining ε_min can be understood as smoothing the spectrum by finding the optimal value of ε_min. Pseudocode depicted in Figure 3.4 summarizes the above described procedure as a function $\textsc{SmoothingErr}(\varepsilon_\mathrm{min}, L_\mathrm{LL}, L^{\downarrow})$ evaluating the error between Planck's law and estimated spectral radiance. This function is minimized with respect to the variable ε_min as follows:

$$\underset{\varepsilon_\mathrm{min}\in[0.6,1]}{\arg\min}\ \textsc{SmoothingErr}(\varepsilon_\mathrm{min}, L_\mathrm{LL}, L^{\downarrow}).$$

Continuous curves in Figure 3.3 show the optimal brightness temperature and emissivity relationship approximation. Let us emphasize that by applying emissivities obtained from the approximated relationship between brightness temperature and emissivity to eq. (3.5), one gets L' as the best fit to Planck's law. This means that $B^{-1}(L'_i)$ produces a temperature value for each band. These temperatures have minimum variability since they are derived from the best fit to Planck's law. Let us also remind the reader that maximum brightness temperature is coupled with emissivity equal to 1, which implies that it is a part of the set of temperatures with smallest variability. It is important to note that maximum brightness temperature T_b computed from land-leaving radiance is usually smaller than surface temperature T computed from surface radiance. Land-leaving radiance is smaller than surface radiance since natural materials are of emissivity higher than 0.6 and the contribution from reflected downwelling radiance is usually much lower than surface radiance. By reason of maximum brightness temperature T_b being smaller than surface temperature T and by being part of the set of temperatures with smallest variability, it can be concluded that maximum temperature from the set of temperatures tends to be the closest to the surface temperature T and is therefore taken as the reference one.

Function SmoothingErr($\varepsilon_{\min}, L_{\mathrm{LL}}, L^{\downarrow}$)

1. $T_{\mathrm{b}_i} = B^{-1}(L_{\mathrm{LL}_i})$
2. Find p and q by solving
   $$1 = p \max(T_{\mathrm{b}_i}) + q$$
   $$\varepsilon_{\min} = p \min(T_{\mathrm{b}_i}) + q$$
3. Estimate emissivity
   $$\varepsilon_i = p\, T_{\mathrm{b}_i} + q$$
4. Estimate spectrum
   $$L'_i = \frac{L_{\mathrm{LL}_i} - (1-\varepsilon_i) L_i^{\downarrow}}{\varepsilon_i}$$
5. $T_{\max} = \max(B^{-1}(L'_i))$
6. **return**
   $$\sum_i \left| \frac{B_i(T_{\max})}{||B(T_{\max})||_1} - \frac{L'_i}{||L'||_1} \right|$$

Figure 3.4: Pseudocode of the function that is being minimized in order to estimate the value of $\varepsilon_{\min}$.

Before passing emissivity to the Ratio and MMD modules, it is recomputed according to the following equation:

$$\varepsilon_i = \frac{L_{\mathrm{LL}_i} - L_i^{\downarrow}}{B_i(T) - L_i^{\downarrow}}, \tag{3.6}$$

where T is the maximum temperature associated with optimal $\varepsilon_{\min}$. Equation (3.6) is derived from eq. (3.1) and it is important for relating temperature and emissivity. This recomputation keeps temperature and emissivity consistent with each other (i.e. the same temperature can be derived from any emissivity band). The emissivity is then further processed with the Ratio and MMD modules, with minor changes to the original version of the TES algorithm as it is described in [24] and [25]. These changes include: 1) there is no refinement of $\varepsilon_{\max}$ according to the emissivity spectral contrast, 2) the threshold T_1 for separation emissivities with small spectral contrast is not applied, and 3) the number of MMD iterations is set to one. Let us emphasize that before reporting algorithm outputs, emissivity is recomputed by eq. (3.6) using the final value of temperature.

4

OSTES validation

The OSTES algorithm was tested on both synthetic and real data. Synthetic data were generated from spectral and climatological libraries such that they cover many possible scenes and conditions. These data were simulated as would be acquired with ASTER, AHS and TASI sensors. The OSTES was further tested on a real data. For this purpose image data acquired by ASTER and TASI sensors were chosen. The ASTER image data include water bodies of the Caspian Sea and Lake Baikal. The TASI image data contain urban areas of city of Brno.

4.1. Synthetic data

Imaging systems

Synthetic data are intended to cover many possible situations of acquiring thermal data. Therefore three different sensor architectures were chosen to test the OSTES algorithm and compare the results with the TES algorithm.

From the wide range of airborne sensors operating in the TIR region two are chosen as examples: the AHS operated by Spanish Institute of Aeronauics (INTA) and developed by ArgonST (Fairfax, USA), and the TASI sensor. These sensors offer data of great importance in applications. Notable studies include areas of mineral mapping [47], soil moisture estimation [58], urban studies [63], soil organic carbon estimation [48] and crop water stress characterization [49], among others.

The above-mentioned airborne sensors were chosen together with the ASTER sensor to analyze the performance of the OSTES algorithm. ASTER consists of 15 bands of which 5 are situated in TIR region with (NEΔT) $\approx 0.3\,\mathrm{K}$. The spatial resolution of the TIR bands is 90 m. The AHS sensor has been fully operational from 2005 [18]. Its sensor operates in 80 spectral bands where the last 10 bands cover atmospheric window from 8 to 13 µm [61]. The AHS TIR bands have a (FWHM) $\approx 0.5\,\mu\mathrm{m}$ with NEΔT $\approx 0.5\,\mathrm{K}$. The third sensor we will consider is the TASI sensor. It contains 32 bands all of which are in the TIR region. Bands are situated in the 8 to 11.5 µm region and have a FWHM $\approx 0.11\,\mu\mathrm{m}$ with NEΔT $\approx 0.1\,\mathrm{K}$. The response functions of these sensors are depicted in Figure 4.1.

Data set

A data set of 6588 samples was artificially created to compare the performance of the TES and OSTES algorithms. Samples include 108 different natural surfaces chosen from

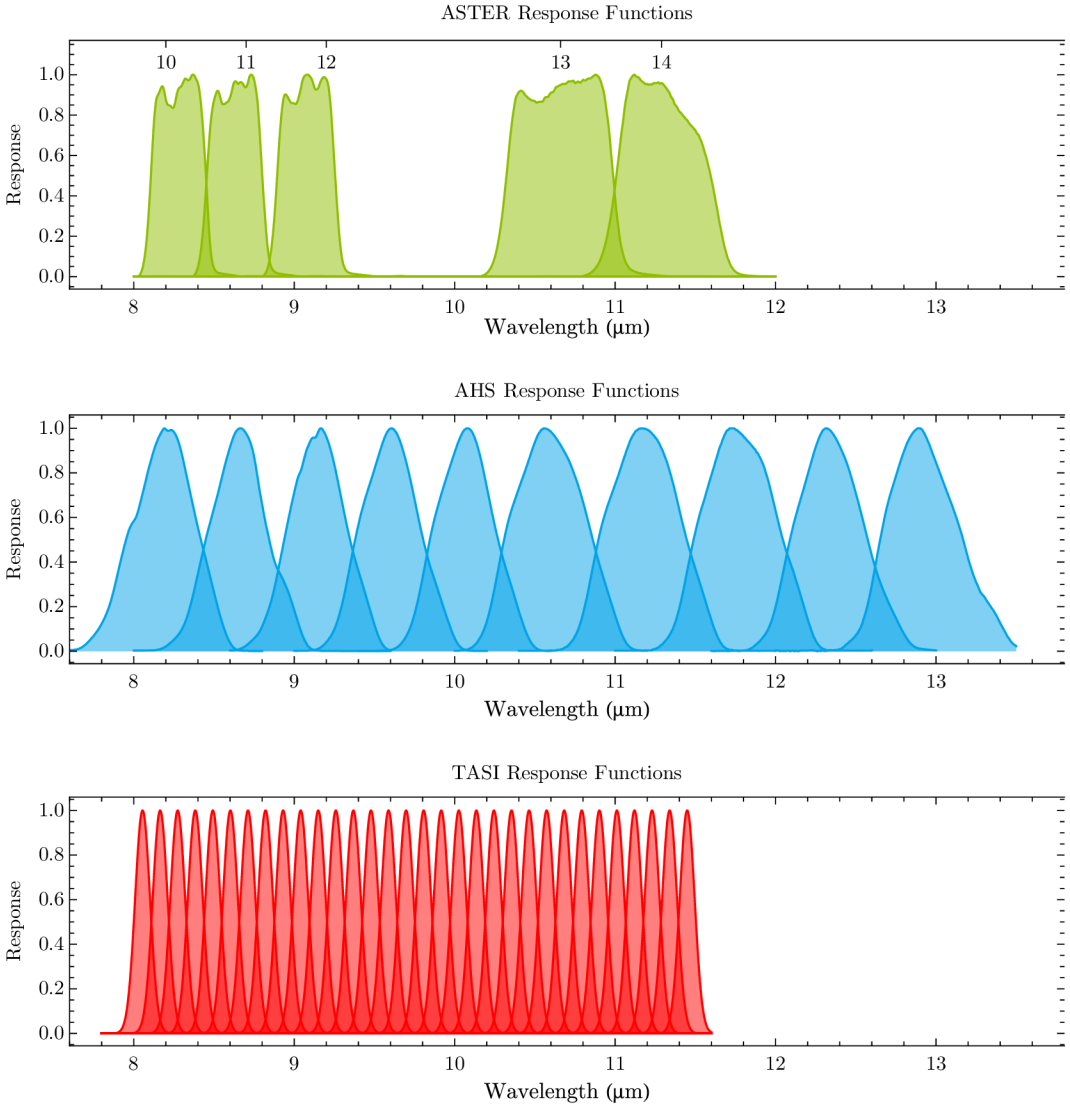

Figure 4.1: Response functions for ASTER, AHS and TASI sensors. The ASTER Band Numbers are shown above the ASTER response functions.

ASTER spectral library [6] at different temperatures coupled with 61 different atmospheric conditions taken from TIGR (TOVS Initial Guess Retrieval) database [14, 13]. Sample temperatures range from 244 K to 310 K. In order to simulate real conditions, every sample at a certain temperature is coupled with a certain type of atmosphere. The chosen atmospheres represent a variety of possible conditions within polar, mid-latitude and tropical airmasses. These samples were processed to land-leaving and downwelling radiance, as standard TES algorithm input, and they were transformed to band-effective quantities with respect to the ASTER, AHS and TASI response functions. Samples were passed to the algorithms individually.

Sensor	a	b	c	r^2
ASTER	0.994	−0.687	0.737	0.983
AHS	1.000	−0.782	0.817	0.994
TASI	1.001	−0.737	0.760	0.997

Table 4.1: Regression coefficients of $\varepsilon_{\min} = a + b\,\mathrm{MMD}^c$ and coefficients of determination r^2.

Simulated data for the ASTER sensor were processed with the current implementation of TES, as it is used for generation of ASTER standard products AST_05 and AST_08 [5]. The version of the original TES algorithm in cases of AHS and TASI sensors was implemented in a manner similar to that described in [39]. In addition, the implementation omits the $\varepsilon_{\max}$ refinement for emissivities with low spectral contrast. The OSTES was applied to all sensors as it is described in section 3.2.

Let us remind the reader that the regression coefficients in the eq. (3.2) need to be refined for each sensor with respect to its response functions. The regression coefficients in eq. (3.2) were recomputed for AHS and TASI sensors using their respective response functions. In both cases the regression was performed on a set of 108 spectra chosen from same categories and library as in the ASTER case. The coefficients for different sensors are shown in the Table 4.1.

Validation

Samples were passed to the TES and OSTES algorithms and the temperature and emissivity results were compared with true values. We divide the results into two groups according to the emissivity spectral contrast. For each sensor type we determined a threshold for Maximum-Minimum emissivity Difference (MMD) in order to separate the samples with small spectral contrast such as water, vegetation, snow or samples with small particle sizes from other samples with higher spectral contrast. The threshold was determined for each sensor separately since different response functions and spectral ranges result in different MMD values for the same sample. The performance of both TES versions was determined by subtracting retrieved temperature from true temperature value. The temperature error and chosen MMD values for ASTER, AHS and TASI are shown in Figure 4.2.

Note that the temperature retrievals using OSTES are both more accurate and more precise than TES in the case of samples with low spectral contrast. It is also important to note that no significant improvement is evident for samples with higher spectral contrast.

Let us remind the reader that every sample is processed under several different atmospheric conditions coupled with different sample temperatures. Thus the standard deviation of temperature and emissivity error is indicative of the algorithm's sensitivity to seasonal fluctuations. A comparison of standard deviations of temperature errors introduced by both TES approaches reveals that the OSTES is less sensitive to changes in atmosphere and sample temperature for samples with low MMD. However, the standard deviations of temperature errors of samples with higher MMD are similar. Standard deviations of temperature errors obtained by the OSTES and TES algorithms are summarized in the Table 4.2.

Sensor	MMD	OSTES	TES
ASTER	< 0.021	0.25	0.50
	> 0.021	0.36	0.43
AHS	< 0.052	0.13	0.20
	> 0.052	0.20	0.19
TASI	< 0.026	0.16	0.32
	> 0.026	0.32	0.30

Table 4.2: Standard deviations of temperature errors obtained by applying OSTES and TES algorithm on simulated data as seen by ASTER, AHS and TASI grouped according to the sample Maximum-Minimum emissivity Difference (MMD).

4.2. Comparison with ASTER standard products

The OSTES temperature and emissivity were compared with ASTER standard products AST_08 (kinetic temperature) and AST_05 (surface emissivity). For this purpose scenes containing water bodies were chosen. Water emissivity is well-known and does not vary significantly which offers a unique opportunity for testing various algorithm features. Water bodies are commonly used for calibration [69, 66] and validation [68, 67] purposes.

Testing was focused on: 1) investigating the impact of various atmospheric conditions on emissivity retrievals of the same material, and 2) emissivity smoothness over homogeneous areas. Both tests were performed on ASTER scenes containing large water bodies, since water emissivity is well-known. For the first test we chose five scenes of the Caspian Sea acquired in various seasons of the year. For the second test we chose Lake Baikal. The list of all scenes used, together with their acquisition and processing dates, is given in Table 4.3. For every scene we downloaded ASTER standard products AST_09T, AST_08 and AST_05 delivering land-leaving and downwelling radianace, surface kinetic temperature and surface emissivity, respectively. Product AST_09T was used as input to the OSTES algorithm. The resulting temperatures and emissivities were then compared with

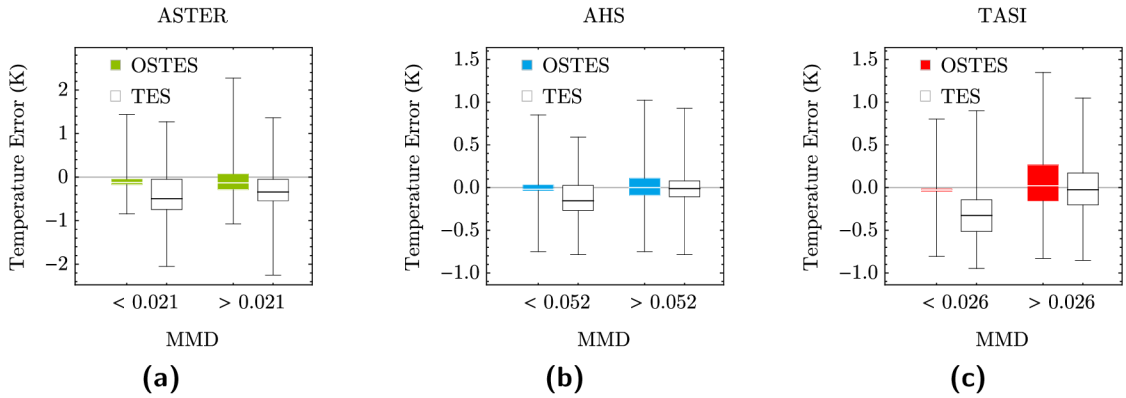

Figure 4.2: Box plots representing temperature error produced by OSTES and TES algorithms for ASTER, AHS and TASI sensors. Results are divided in two groups based on the Maximum-Minimum emissivity Difference (MMD) in order to demonstrate the improvement of the OSTES algorithm. Whiskers represent minimum and maximum of temperature error.

Location	Acq date (UTC)	Processing date	Precipitable water [$\mathrm{kg\,m^{-3}}$]
Caspian Sea	11.02.2001 - 07:35:55	19.11.2015	9
Caspian Sea	29.06.2002 - 07:31:47	19.11.2015	30
Caspian Sea	21.08.2004 - 07:29:35	19.11.2015	21
Caspian Sea	30.09.2001 - 07:35:57	19.11.2015	28
Caspian Sea	13.11.2008 - 07:24:21	19.11.2015	10
Lake Baikal	22.07.2002 - 04:17:29	27.08.2015	18

Table 4.3: ASTER scenes used for algorithm testing

the AST_08 and AST_05 standard products. The emissivity variability over large and homogeneous water bodies was chosen to be the quality indicator, since we are interested in the retrieval of material properties, which should be essentially constant over time and space.

Caspian Sea

From the Caspian Sea scenes we chose samples of size 40×40 pixels over uniform, cloudless waterbody. These subsets were processed by the OSTES algorithm and the emissivity results were averaged for every scene. The results are plotted in Figure 4.3 along with the emissivities that were delivered in the AST_05 product and averaged over the same spatial subset. In most cases the AST_05 emissivity spectra appear to be closer to the sea water emissivity spectra taken from ASTER spectral library [6]. However, the temperature retrievals of extracted samples obtained by OSTES and TES are very close (not shown). The average temperature difference of AST_08 and OSTES results computed from all Caspian Sea samples is 0.2 K (s.d. 0.2 K). The fact that the temperatures obtained with the two algorithms are very close, but the emissivities are not implies that the emissivity spectra from AST_05 product are not consistent with temperature from AST_08 product. We verified this inconsistency by taking the temperatures delivered in AST_08 and the downwellig and land-leaving radiances delivered in AST_09T and putting these into eq. (3.6) to obtain emissivities that are different from what is in the AST_05 product. These emissivity spectra derived from AST_08 and AST_09T, which we refer to as "recomputed emissivities", are depicted on Figure 4.3 as well.

Comparison of recomputed emissivity spectra with OSTES emissivity retrievals shows that the spectra are nearly identical in scenes acquired on 29.6.2002 and 30.9.2001. Agreement between these emissivity spectra are the consequence of similar AST_08 and OSTES temperatures; the average difference is -0.04 K (s.d. 0.15 K). It may be important to note that these scenes contain clouds in areas adjacent to the processed sample. On the other hand OSTES results perform slightly better in scenes acquired on 11.2.2001, 21.8.2004 and 13.11.2008. The average temperature difference between AST_08 and OSTES in these scenes is 0.28 K (s.d. 0.13 K). Nevertheless, none of the emissivity spectra agrees with expected values.

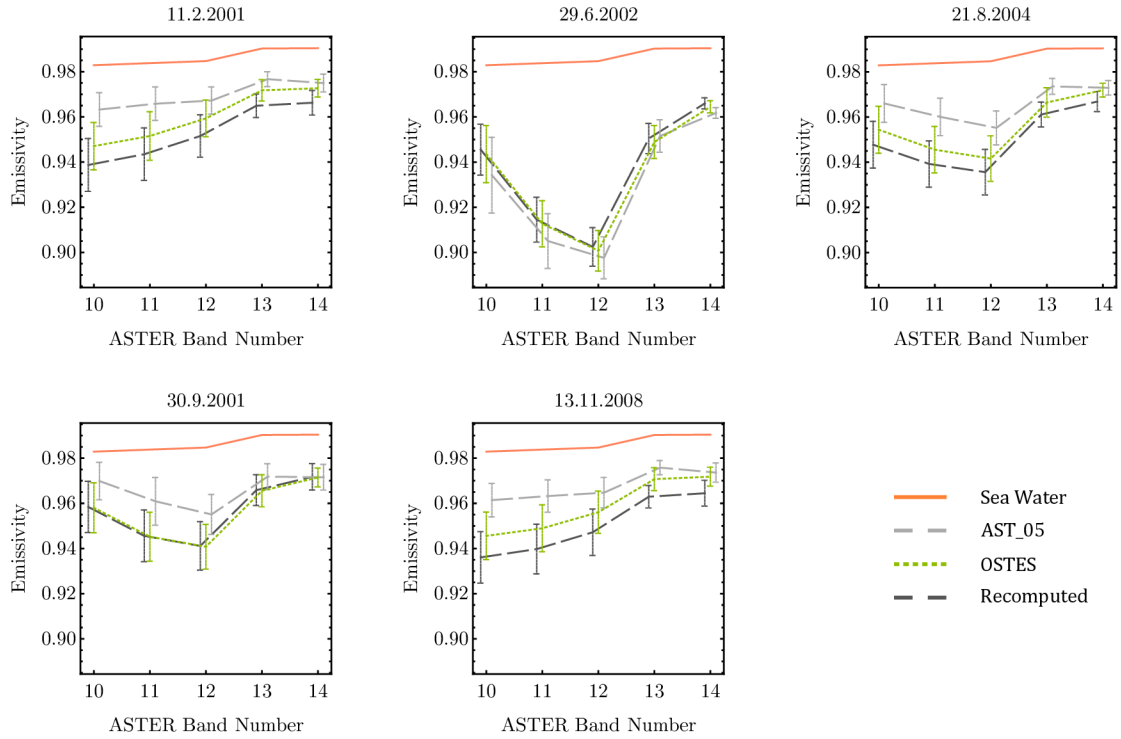

Figure 4.3: Emissivity of Caspian Sea in different seasons obtained from the ASTER standard product AST_05, OSTES retrieval, and emissivity recomputation according to the temperature from AST_08 and land-leaving and downwelling radiance from AST_09T. Emissivities were extracted from an area of size 40×40 pixels over pure and cloudless waterbody. Error bars display standard deviation.

Lake Baikal

The difference in emissivity obtained by the two versions of TES is further illustrated in the scene over Lake Baikal shown in Figure 4.4. In this figure the white squares on the images define a water body sample of size 90×90 pixels that was used to produce the values in the histograms below the images. The expected values of sea water emissivity (red vertical line) are included in the Figure 4.4. The histograms show the OSTES emissivity retrievals compared against the AST_05 standard product, as well as the emissivity recomputed with respect to the temperature delivered by AST_08 and land-leaving and downwelling radiance delivered by AST_09T, as described in the previous paragraph. Inspection of the ASTER standard product AST_05 shows that emissivity values in bands 10, 11 and 12 over the homogeneous study sample are clustered around two distinct values. This creates step discontinuities which are reflected in the bimodal distributions in the histograms and in the noisy patterns in the top image. This will be discussed further below. In contrast to AST_05 emissivities, OSTES emissivity results are smoother and the histograms do not show any significant bimodality. The recomputed and OSTES emissivity retrievals are similar. However, the OSTES emissivities tend to be closer to the expected values. In addition to the noise, striping is also visible in the images. Striping is caused by electronic noise and can distort emissivity spectra by triggering thresholds included in the original TES algorithm. This can cause step discontinuities. Temperature retrievals are not significantly affected. Striping is more thoroughly discussed in [23]. Even though

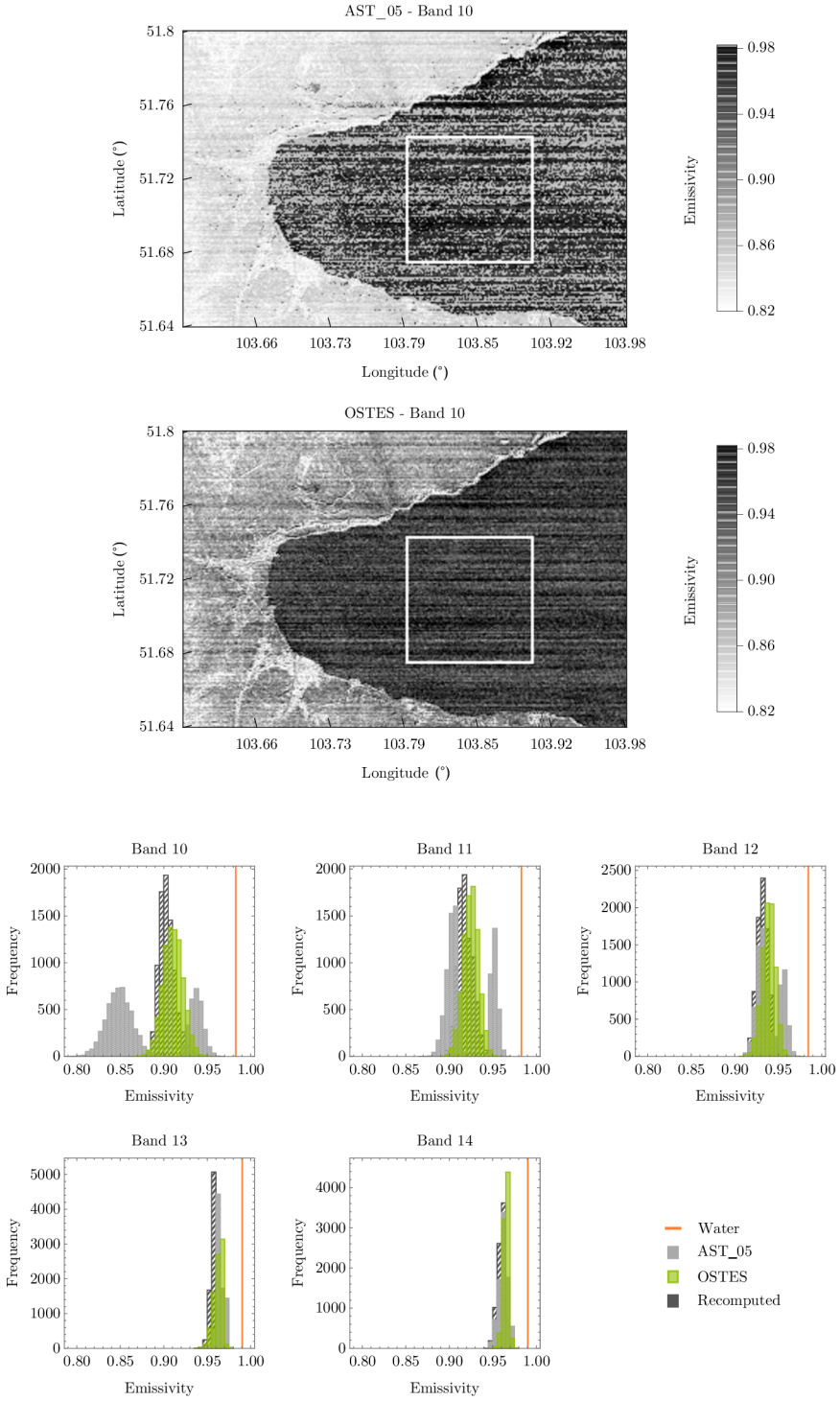

Figure 4.4: ASTER band 10 emissivity images of Lake Baikal obtained from ASTER standard product AST_05 (top) and OSTES emissivity retrieval (middle). In both images the same contrast stretching is used. The white square represents the area from which emissivity histrograms were created (bottom panel). Histograms show distributions of AST_05 emissivity, OSTES emissivity and recomputed emissivity according to the temperature from AST_08 and land-leaving and downwelling radiance from AST_09T. The vertical line depicted in histograms indicates the expected value of water emissivity retrieved from ASTER spectral library [6].

the AST_05 and OSTES emissivities differ significantly in some bands, the temperature retrievals are very similar. The average difference is 0.25 K (s.d. 0.18 K). Similar to the discussion regarding Caspian Sea emissivity retrievals, it can also be concluded in this case that none of the emissivity spectra have satisfying values.

The discrepancies in shape and magnitude of emissivity spectra can be the result of various sources of error but the main error source has been attributed to imperfect atmospheric corrections [67, 68]. Table 4.3 indicates the amount of precipitable water in the atmosphere for each of the investigated scenes. These values were obtained from NOAA's Climate Forecast System Reanalysis. It can be observed that discrepancies in emissivity spectra are related to amount of precipitable water in the atmosphere. Notable works discussing emissivity retrievals over agricultural areas and water bodies are [17, 59]. One suggested improvement is the water vapour scaling method [66, 23].

The step discontinuities in emissivity values over homogeneous areas can occur due to various thresholds deciding how to treat the sample during processing. The original TES algorithm starts in the NEM module assuming a maximum emissivity spectra $\varepsilon_{\max} = 0.99$. The NEM module is then restarted with refined $\varepsilon_{\max}$ according to the emissivity retrieved from the first NEM pass. When the NEM iterations do not converge, then the correction for downwelling radiance is not possible, and obtained values of temperature and emissivity are reported as final. The original version of TES processes samples according to the MMD of emissivity spectra obtained from the NEM module either by incorporating eq. (3.2) or by presetting emissivity to $\varepsilon = 0.983$. Some authors [27], [54] have suggested that the value of the threshold used for classifying observations into groups with either low or high spectral contrast should be changed or completely removed. Observations with wrongly determined spectral contrast or observations with spectral contrast close to any threshold result in step discontinuities. By comparison, the OSTES does not set any thresholds for materials with low spectral contrast and so it is expected to generate smoother results on homogeneous areas with low spectral contrast.

4.3. Application to TASI image data

The OSTES algorithm was applied on image data acquired by TASI sensor and the results were compared with emissivities obtained from *in-situ* mesaurements and the TES algorithm esmissivity estiamtions.

Experiment setup

The study was performed using data acquired over the city of Brno, Czech Republic (lat: 49.2, lon: 16.6). The examined data are subset of a flight line crossing the city from south-west to north-east. The acquisition was performed on 4.7.2015 at 14:03 (UTC). The FLIS operated by Global Change Research Institute CAS (Brno, Czech Republic) [28] was used for this acquisition. FLIS consists of Compact Airborne Spectrographic Imager (CASI), Shortwave infrared Airborne Spectrographic Imager (SASI) and TASI sensor. All sensors are developed by Itres Ltd. (Calgary, Canada).

In-situ measurements of urban materials were performed with Fourier transform infrared (FTIR) Spectrometer Model 102 developed by D&P Instruments (Simsbury, USA). The emissivity of measured surfaces was estimated by a spectral smoothing algorithm,

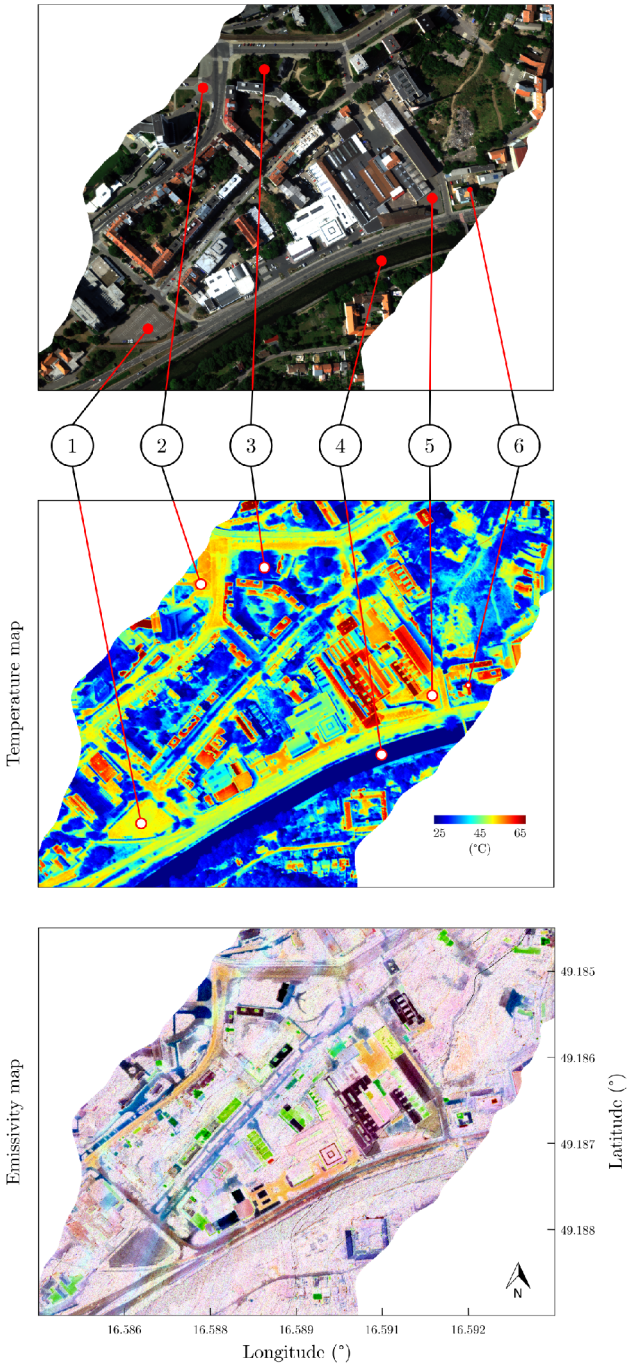

Figure 4.5: Part of flight line over the city of Brno. Image data were acquired on 4.7.2015 at 14:03 (UTC). The top image displays true color image of the studied area. The middle image is a temperature map obtained from the OSTES algorithm applied on image data from the TASI sensor. The bottom image is false color emissivity map obtained from OSTES algorithm (red - band 10, green - band 15, blue - band 20). On the top and middle images locations and labels of *in-situ* measurements are shown. Labels refers to following surface types: 1 - asphalt hotel parking, 2 - concrete blocks, 3 - vegetation, 4 - Svratka river, 5 - asphalt parking lots and 6 - asphalt rooftop.

which is different than spectral smoothing algorithm described in Section 3.1. Principles of these algorithms are similar but the one applied on FTIR data depends on high spectral resolution and neglects atmosphere along the line of sight. This algorithm is discussed in detail in [31]. Emissivity spectra of water and deciduous trees were not measured but instead they were extracted from ASTER spectral library [6]. All emissivity spectra were resampled with respect to TASI response functions. The study area and locations of the *in-situ* measurements are shown in the upper part of the Figure 4.5.

Spectral emissivity libraries are very useful for calibration and validation purposes. Let us emphasize that there are many other spectral emissivity libraries available apart from ASTER spectral library. Notable libraries are Johns Hopkins University Spectral Library [55], Arizona State University Spectral Library [15], United States Geological Survey Spectral Library [16] and the Spectral Library of Urban Materials (SLUM) [43]. In the Appendix A is described a spectral emissivity library which is specifically focused on spoil substrates.

The OSTES implementation in the TASI processing chain

Image data acquired by the TASI sensor were radiometrically, atmospherically and gemetrically pre-processed as described the Chapter 2. The result of the pre-processing is land-leaving radiance, which is the first input parameter for the OSTES and the TES algorithm. The second input parameter to both algorithms is downwelling atmospheric radiance. This quantity was obtained from the radiative transfer model MODTRAN [8]. MODTRAN requires temperature and water vapour profiles, which were extracted from MOD07_L2 product [9] generated from MODIS image data.

The described procedure of temperature and emissivity estimation from pre-processed TASI image data is the continuation of the processing chain introduced in Chapter 2. The schematic illustration of the OSTES implementation into the processing chain of the TASI image data is depicted in the Figure 4.6, which is the continuation of the processing chain depicted in the Figure 2.2. The whole processing chain of TASI image data described in this work is operational at Global Change Research Institute CAS (Brno, Czech Republic).

The processing of the TASI image data acquired during this experiment was limited to 22 spectral bands. First five and last five spectral bands were not considered since they were most affected by imperfect atmospheric corrections.

The TASI image data were processed by the TES and OSTES algorithms in order to compare the temperature and emissivity retrievals. The TASI image data were processed with the TES algorithm by substituting OSTES algorithm in the processing chain of TASI image data. The implementation of the TES algorithm is based on the implementation described in [39] without the $\varepsilon_{\max}$ refinement for emissivities with low spectral contrast.

Comparison

Temperature and emissivity results of the OSTES algorithm are depicted in the middle and lower part of Figure 4.5 in the form of temperature and emissivity maps. The temperature map shows high temperature differences between vegetated and built areas. Emissivity map is a false color composition (red - band 10, green - band 15, blue - band 20) showing variability of surface materials in the image data.

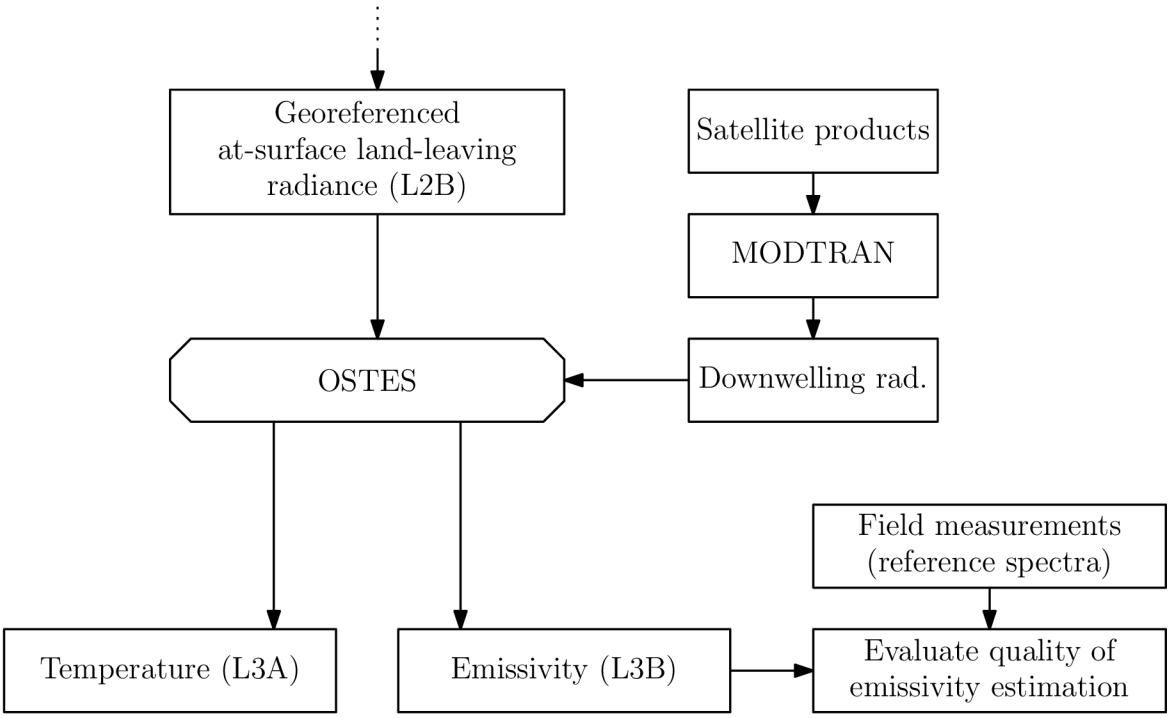

Figure 4.6: Continuation of the processing chain of the TASI image data introduced in the Chapter 2 and depicted in the Figure 2.2. This part illustrates temperature and emissivity separation processing chain applied to the pre-processed TASI image data.

The *in-situ* measurements were not performed during the overflight. Therefore temperature could not be used for the comparison and the validation of the TES and OSTES algorithms. The comparison of the TES and the OSTES algorithms' performance was tested against six emissivities obtained from *in-situ* measurements. Results are shown in the Figure 4.7, where error bars display standard deviation. Both TES and OSTES emissivity retrievals are very similar. The OSTES performs slightly better than TES in cases of deciduous trees and the river of Svratka. However, neither of these two spectra agrees with the shape and magnitude of the expected emissivity spectra. These discrepancies can be caused by various sources of errors but the main error source has been attributed to the imperfect atmospheric corrections. Emissivities of the spot 5, asphalt parking lots, retrieved by the TES and OSTES significantly differ from *in-situ* measurement. This shift in magnitude is introduced by the insufficient compensation of the downwelling radiance. This spot is surrounded by buildings, which increase the amount of downwelling radiance. This additional radiance is not included in the atmospheric parameters retrieved from MODTRAN. The rest of the emissivity retrievals are considered to follow *in-situ* measurements well. Let us emphasize the reader that OSTES offers only moderate improvements in emissivity retrievals. These are not possible to observe in this comparison due to the magnitude of the error introduced by the imperfect atmospheric corrections.

These data were acquired within a campaign focused on detecting urban heat island of the city of Brno. The main goal was determination of parameters affecting temperatures in the city. Preliminary observations are introduced in the Appendix B.

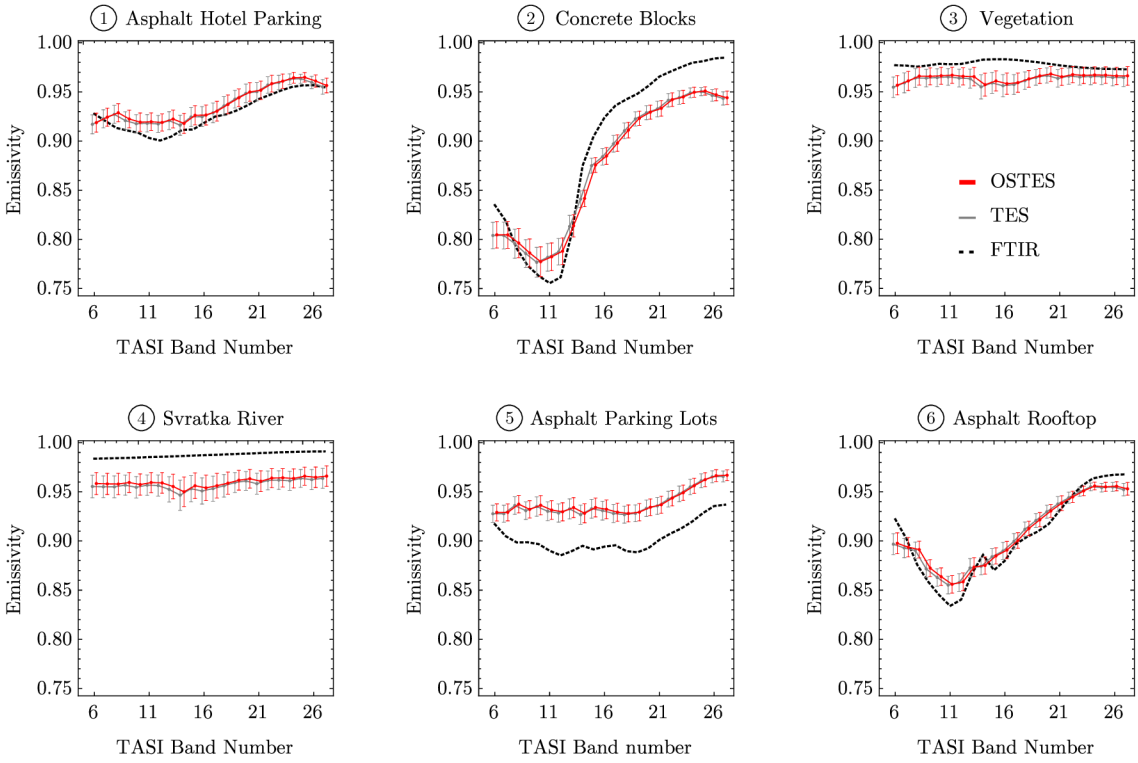

Figure 4.7: Comparison of TES and OSTES emissivity retrievals with emissivities obtained from *in-situ* measurements. Error bars display standard deviation.

5

Conclusion

Thermal hyperspectral data delivers unique information about temperature and emissivity of the Earth surface which is used in many application in both scientific and commercial fields. However, derivation of these quantities leads to the underdetermined system of equations, as was discussed in the Chapter 3. Many approaches have been developed to overcome this problem among which the TES algorithm is the most widely known and used.

The TES algorithm is well established and popular for several reasons: it retrieves temperature and emissivity of natural surfaces simultaneously without any previous knowledge of surface type and it is widely applicable to range of multispectral and hyperspectral sensors. This suggests that the algorithm is a good benchmark for temperature and emissivity separation. Any improvement to the TES algorithm can benefit processing of thermal data from many sources.

Chapter 3 introduced a module that estimates temperature and emissivity from an approximation of the relationship between brightness temperature and emissivity. The new module replaces the NEM module in the original TES to create an algorithm that we call OSTES. The OSTES algorithm was chosen for processing image data acquired from TASI sensors operated by Global Change Research Institute CAS (Brno, Czech Republic). The pre-processing chain is applied to the image data before passing them to the OSTES algorithm. The individual pre-processing steps were described in the Chapter 2 and the attachment of the OSTES to the pre-processing chain is discussed in the Chapter 4.

The performance of OSTES was firstly tested on a set of simulated data recomputed with respect to ASTER, AHS and TASI response functions. Results show that temperature estimations using OSTES are more accurate and precise than TES for samples with low spectral contrast. It should be noted that this improvement is of modest size when compared to the already accurate results that can be obtained with TES. OSTES and TES perform similarly for samples with a high spectral contrast. The results also reveal that OSTES is less sensitive to variations in atmospheric conditions.

The OSTES was also compared against the ASTER standard product AST_09T over the Caspian Sea and Lake Baikal. By comparing the OSTES results to ASTER standard products AST_08 (temperature) and AST_05 (emissivity) we found that temperature retrievals of both algorithms are very similar. However, it was also found that temperatures included in the AST_08 product are not consistent with emissivities delivered by AST_05 product in the sense of eq. (3.6). Thus emissivities were recomputed based on downwelling and land-leaving radiance from AST_09T and temperature from AST_08.

Comparing all three emissivity retrievals over the Caspian Sea in different seasons shows that emissivity from AST_05 to be closest and recomputed emissivity to be the fur-

thest from expected sea water emissivity values extracted from ASTER Spectral Library, except of those in the June and September scenes, which are expected to have the largest water vapour burden in the atmosphere. It is also observed that the AST_05 emissivities over Lake Baikal exhibit step discontinuities. In the same region OSTES and recomputed emissivities tend to be smoother with OSTES emissivities being closer to expected value of water emissivity. All emissivity retrievals are probably affected by inaccurate atmospheric corrections since none of the obtained spectra had emissivity values close to expected values.

The performance of the OSTES and TES was tested on image data acquired by TASI sensor and validated against *in-situ* measurements. The emissivity retrievals from both algorithms follow *in-situ* measurements well in most of the cases.

We conclude that improvements in atmospheric compensation will be crucial for further improvements in emissivity results. Thus, further work should be focused on this topic. Additional improvements in OSTES will consider modifications of cost function represented in eq. (3.3) and illustrated in Figure 3.4. Better approximations of the relationship between brightness temperature and emissivity should result in better temperature and emissvity retrievals.

The OSTES algorithm is preferred mainly because of higher precision and accuracy under conditions of low spectral contrast, and because of the consistency between retrieved temperature and emissivity. We believe that implementing OSTES to processing chain of TASI image data will benefit application for landscape assessment. We also hope that improvements introduced by OSTES will help to enhance the quality of temperature and emissivity results in general.

Appendices

A

Spectral emissivity library of spoil substrates

Spectral emissivity libraries contains valuable information about Earth surface materials, which can be utilised for validation and calibration purposes of airborne or satellite image data. Several libraries are currently available among which is also a spectral emissivity library of spoil substrates [2]. This appendix introduces mentioned library in detail.

A.1. Introduction

Post-mining sites represent areas of large-scale and intensive disturbance. They can have significant impacts on the surrounding landscape in many countries of the world. Original ecosystems can be damaged or destroyed, and the restoration of ecosystem functions and services is necessary [12]. Afforestation is widely used reclamation method. Many studies demonstrate that post-mining sites have a large potential for carbon sequestration if afforestation has been applied [72, 20, 56, 70]. This can contribute to mitigate the current increase in atmospheric CO_2 concentrations.

During opencast mining a large amount of substrate above the coal layer is removed and relocated in heaps covering extensive areas. These heaps consist of material often excavated from depths of several hundred meters. This material is called spoil substrate and it can vary in its physical and chemical properties. The heterogeneity is largely affected by geology and the method of mining and heaping. For this reason the substrates differ substantially from recent soils. They often have extreme pH and may contain high concentrations of heavy metals, polyphenols (i.e., products of coal decomposition) and salt content. Such properties can significantly impact a success and/or speed of vegetation development at post mining sites. Therefore a proper knowledge on spoil substrate properties and distribution is necessary in land rehabilitation.

Thermal infrared remote sensing can provide beneficial tools for monitoring of post-mining areas. Particularly, land surface emissivity (LSE) can be used for spoil substrates classification. In addition, physical and chemical properties can be estimated by spectral analysis of LSE. Land surface temperature (LST) is closely connected to soil moisture which is important for establishment of new ecosystems. All of this information is required when proper land reclamation should be applied. This can include mainly substrate mechanical treatment, such as trenching in order to regulate water regime, chemical treatment (e.g., liming), and selection of appropriate tree species.

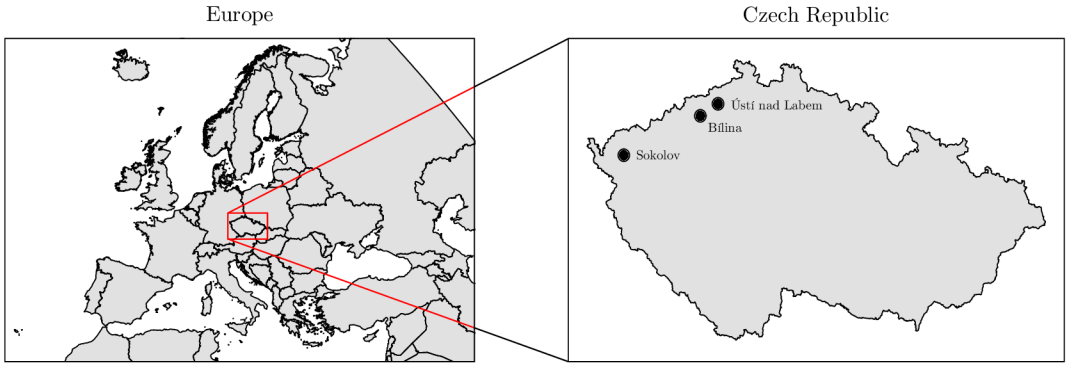

Figure A.1: Locations of brown coal mining sites from which spoil substrate samples were extracted.

LST is coupled with LSE and thus one quantity cannot be derived without knowledge of the second. These quantities cannot be explicitly derived from radiance measurement. The reason is that by observing radiance in N bands one gets N unknown emissivities plus one unknown temperature. Such a system of equations is underdetermined (i.e., more unknown than known variables). Several algorithms have been suggested to solve this problem [44]. These algorithms either require knowledge of LSE in advance, or an estimate LSE as a part of their output. A library of spectral emissivities can be utilized for: 1) determination of LST, 2) material classification, and 3) LSE validation of airborne and satellite thermal remote sensing data.

This work describes a spectral library of spoil substrate emissivities from brown coal mining sites in the Czech Republic near towns of Sokolov, Chodov, Bílina and Ustí nad Labem (Figure A.1). The spectral library contains emissivities, soil pH in water and in KCl, soil conductivity, content of water soluble Na and K, Al and Fe in KCl, loss on ignition and content of polyphenols. In addition to all measured physical and chemical parameters, sample's latitude and longitude are listed. The dataset consists of 24 spoil substrate samples, which were homogenized by mixing and sieving before any sample analysis. The toxicity test and measurement of chemical properties are discussed at length in [19]. Data collection for emissivity retrievals was performed outdoors in Petri dishes using a FTIR spectrometer Model 102 (D&P Instruments, United States). The emissivity of each sample was estimated by a spectral smoothing algorithm [31].

Datasets containing LSE are rare in comparison with datasets containing LST measurements. The most well-known spectral libraries containing emissivities are the ASTER Spectral Library [6], Johns Hopkins University Spectral Library [55], Arizona State University Spectral Library [15], United States Geological Survey Spectral Library [16] and the Spectral Library of Urban Materials [43]. However, these spectral libraries do not include neither geographical coordinates of samples nor representatives of spoil substrates. One example of a spectral library of emissivities from calibration/validation sites containing coordinates for each sample is described in [62]. The dataset described in this paper is exceptional in its nature and location.

The data presented in this paper were used in a study focused on mapping of spoil substrates for site re-cultivation [77] as well as in a study discussing spoil substrates toxicity [19]. The mining site was also mapped with the AHS in visible, near infrared, shortwave infrared and longwave infrared regions for mineral classification purposes [47]. Exam-

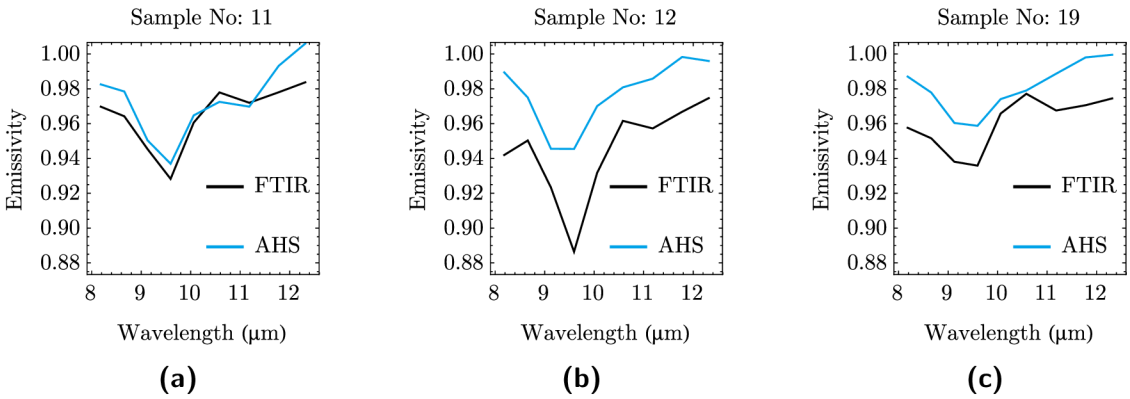

Figure A.2: Examples of corresponding emissivity spectra retrieved from AHS and from spectral library of spoil substrates'. Emissivity spectra from the library were measured by FTIR and they were resampled with respect to AHS response functions.

ples of emissivity spectra retrieved from AHS and their corresponding samples spectra extracted from the library are depicted in Figure A.2. Samples spectra from the library were spectrally resampled with respect to AHS response functions using weighted averages [44]. Comparison of retrieved spectra in case of samples 11 and 19 shows good agreement in shape. Sample 12 exhibits deviations mainly between bands 3 and 4 (9.24 and 9.68 µm). This can be explained by the fact that AHS pixel has 5x5 m pixel size and these pixels were not pure thus had more complex mineral composition than the collected samples. Discrepancies in magnitude can be addressed to imperfect atmospheric corrections or to different soil state during overflight.

Any activity involving remote sensing over these mining sites can benefit from publicly releasing the spectral library of spoil substrates emissivity. Apart from remote sensing application, data in spectral library can be further analyzed for identifying relationships between a sample's spectral emissivity and its chemical properties.

A.2. Methods

The study area is situated around two post mining districts: 1) Sokolov – coal-mining district near towns of Sokolov and Chodov (North-West Czech Republic) and 2) North Czech coal mining district near towns of Bílina and Ustí nad Labem (North Czech Republic). Open-pit mines produce large areas of tailings where spoil material was sampled. Claylike tertiary sediments dominate in these districts.

Spoil substrates were sampled from bare soil without vegetation. Samples contained negligible amounts of organic matter. Extracted samples were further homogenized by mixing and sieving trough a 2 mm screen. Homogenized samples were divided into two groups, from which the first one was used for chemical analysis and the second one for toxicity testing. Samples set for chemical analysis were air dried and stored in a dark place at room temperature. Soil pH in water and in 1N KCl (which is 74.56 g of potassium chloride diluted in 1000 mL of water [41]) was measured using a pH meter with glass electrode in suspension. The suspension was prepared in 1:5 spoil to water ratio and 1:5 spoil to KCl ratio. Conductivity was measured in filtrated suspension using a conductometer. The suspension was prepared in 1:5 spoil to water ratio. Content of water soluble Na and

K was also measured in filtrated water suspension (1:5 spoil to water ratio) using an ion selective electrode. Both suspensions were left to stay overnight. Al and Fe contents in 1N KCl eluate, (1:5 spoil to water ratio), were determined by spectrophotometer Spectra AA 640 (Varian, Australia). Loss on ignition was measured by burning spoil samples at 600 °C for 5 h h. This process is called ashing. To determine the amount of polyphenols, samples were kept in 80 % ethanol (1:5 spoil to ethanol ratio) and stayed for 24 h. Samples were then filtrated and the polyphenol content was determined spectrophotometrically by Folin–Ciocalteau reagent at a wavelength of 765 nm [29]. Gallic acid was used as a standard for calibration. The polyphenol content was expressed as mg/100g of soil. Toxicity was determined by enchytraeid toxicity test. The test is based on the population growth of pot worms in substrates. The details of the measurement are discussed in [19].

Spoil substrate emissivity measurements were collected with Designs and Prototypes Model 102 (United States) portable FTIR spectrometer. The measurements were performed outdoors under clear sky conditions during two consecutive days in the summer season. The spectroradiometer was pre-heated to maximum expected ambient day temperature during the nights before both measurement days. The samples were positioned on the south side of the spectrometer to avoid shadows. The fore-optic field-of-view was 4.8° and it was 60 cm from the sample. Such a configuration resulted in a spot size of approximately 5 cm. Samples were put in a 14 cm diameter Petri dish and were allowed to be heated up naturally in the sunlight. Sample temperatures ranged from 40 °C to 50 °C. Every sample was measured at three different spots. The measurement of one spot consisted of ten measurements, which were averaged. The resulting emissivity of each sample is the average of all three measurements. Sample temperature and emissivity were determined by a spectral smoothing algorithm, as described in [31].

During the measurements the instrument was calibrated using two blackbodies at different temperatures. A cold blackbody was set to the ambient temperature (30 °C) and warm blackbody was set just above the sample temperature (40 – 50 °C). The calibration procedure during the first four spoil samples was done between the changing of each sample. The calibration procedure during the rest of the measurements was done between every fourth sample. Before every sample a measurement was made of a diffuse gold reflectance plate (Infragold from Labsphere Inc.), to compensate for downwelling radiance, as suggested in [21]. The measurement of one sample along with instrument calibration and measurement of the diffuse gold reflectance plate took around 15 minutes. A description of the procedures for converting instrument response to radiance and compensating for downwelling radiance can be found in [31] and [30].

Some of the spoil substrate emissivity spectra are greater than one at certain wavelengths. This inaccuracy occurs at both ends of provided wavelengths interval (i.e. near 8 µm and near 14 µm). Data at these wavelengths are on the edge of atmospheric window and thus the cause of the inaccuracy is imperfect compensation for downwelling radiance. Samples with numbers 33, 34 and 38 are missing header information of latitude and longitude. Absent values are indicated by ‘NA’ string. In these cases the origin of the sample is specified with respect to closest town (either Bílina or Sokolov). We still find these data meaningful, since they can be used as spectral endmembers.

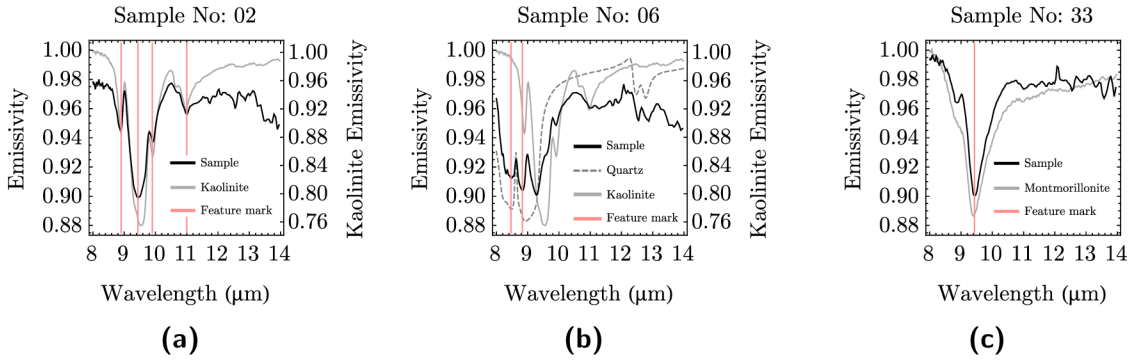

Figure A.3: Spectra of three samples taken from the spectral emissivity library of spoil substrates: (a) sample 02 representing clay rich for kaolinite; (b) sample 06 representing coal combined with sand and clay; (c) sample 33 representing bentonite. Kaolinite and montmorillonite spectra were extracted from Arizona State University Spectral Libary [15] and quartz spectra was extracted from ASTER Spectral Library [6]. Kaolinite spectrum is scaled for clarity reasons.

A.3. Data properties

All of the samples contain varying amounts and types of clay minerals, as evidenced by their spectral emissivity features. Figure A.3 depicts three examples of spoil samples taken from the spectral library. These spectra can be compared with spectra of similar materials extracted from Arizona State University Spectral Library [15] and ASTER Spectral Library [6], which are illustrated in the Figure A.3 as well. Sample 02 (Figure A.3a) is clay consisting mostly of kaolinite with significant dips at 8.90, 9.44, 9.90, and 11.00 µm. Sample 06 (Figure A.3b) is coal combined with sand and clay. The emissivity spectrum of this sample contains kaolinite features mixed with a quartz feature at 8.47 and 8.83 µm. The sample 33 (Figure A.3c) is bentonite rich for montmorillonite. Montmorillonite has typical dip in spectral emissivity at 9.43 µm. The spectral emissivity library of spoil substrates includes also image providing a preview of all samples in library similar to images shown in Figure A.3.

Thermal infrared remote sensing can be used for classification of spoil substrates and for determination of their physical and chemical properties. The spectral library presented in this paper can ease and enhance all these activities. Obtaining this information together with LST is valuable for selection and monitoring of restoration process at post-mining sites.

A.4. Data description

The spectral library consists of 24 ASCII files. Each file describes one spoil substrate. Individual files are named according to the sample number. Files consist of a file header and spectral emissivities. Both file parts are described in the subsections below.

A.4.1. Header

The format of the header is similar to the format of the ASTER Spectral Library header [6]. Each file contains 26 lines of header, which includes available sample information.

The header is divided into four sections separated by empty lines. First part contains 9 lines discussing sample classification, particle size and sample origin. Sample origin is expressed by latitude and longitude on the reference ellipsoid WGS84. This information is summarized in the following fields:

1. Name
2. Type
3. Class
4. Particle size
5. Sample No
6. Owner
7. Origin
8. Latitude
9. Longitude

A second section contains information about sample toxicity and chemical properties. The unit of each quantity is indicated in square brackets after quantity name. This header section contains following fields:

1. toxicity
2. pH in H20
3. pH in KCl
4. conductivity
5. water soluble Na
6. water soluble K
7. Al in KCl
8. Fe in KCl
9. loss on ignition
10. polyphenol content

A third section contains reference to [19], which discusses toxicity measurement and chemical analysis. Finally, the fourth header section contains the names of two columns, in which the following spectral emissivity data are aligned. Metadata in each header line contains an attribute name followed by a colon (ASCII Character 3A) and tab (ASCII Character 09) and then the corresponding value.

A.4.2. Spectral emissivity

After the header part, the file continues on lines 27 – 213 with spectral emissivity data aligned in two columns. As header file indicates, the first column contains wavelength in micrometers and the second column contains corresponding emissivity value. Values in each row are separated by tab. The emissivity of each sample is provided in wavelengths interval from 8 µm to 14 µm. Sampling in this interval is non-linear. Spectral emissivities contained in the spectral library are depicted in Figures A.4 and A.5. Spectral emissivity library is part of the supplementary materials to the manuscript [2].

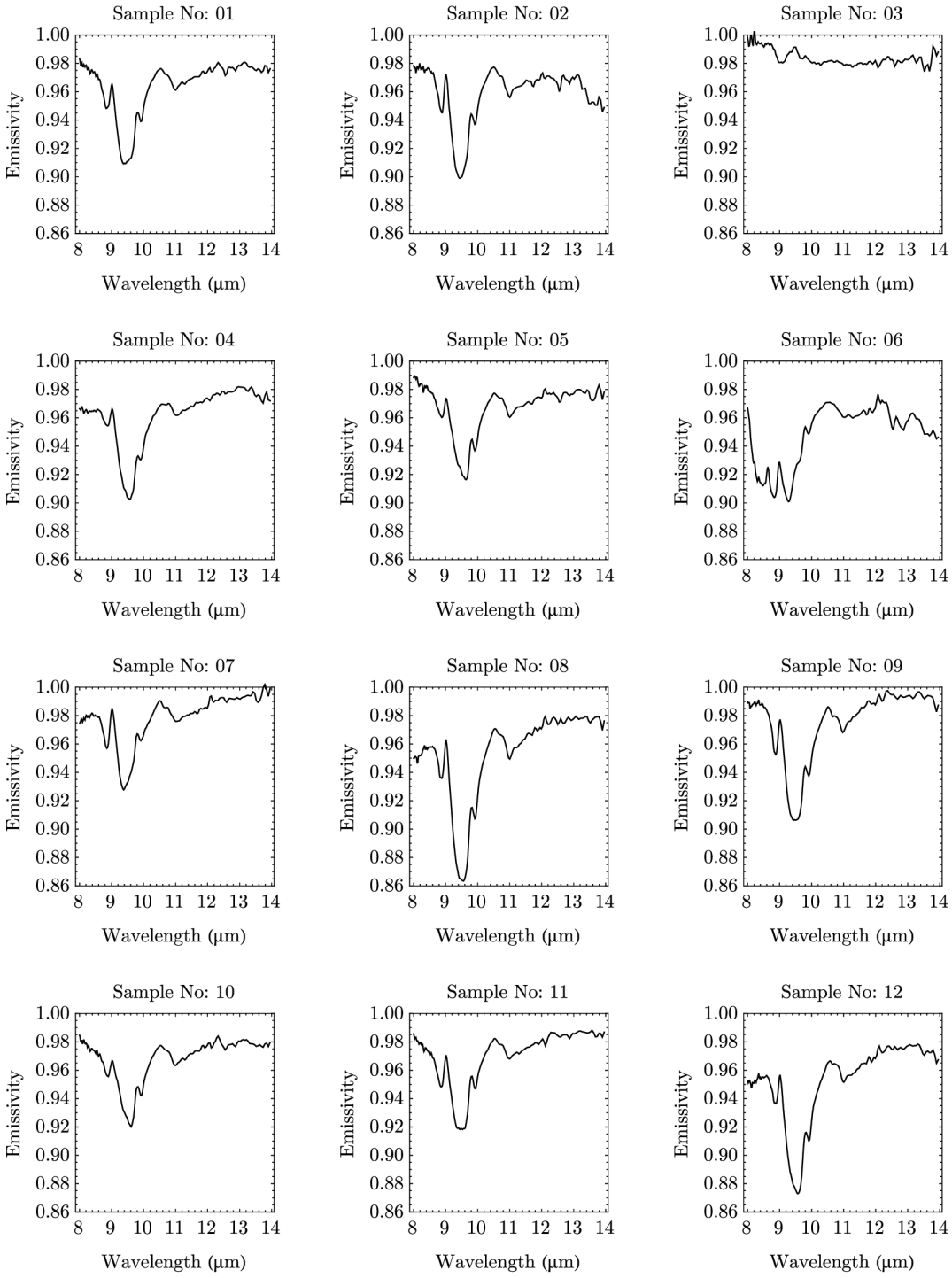

Figure A.4: Depiction of samples' emissivity spectra included in the library of spoil substrates.

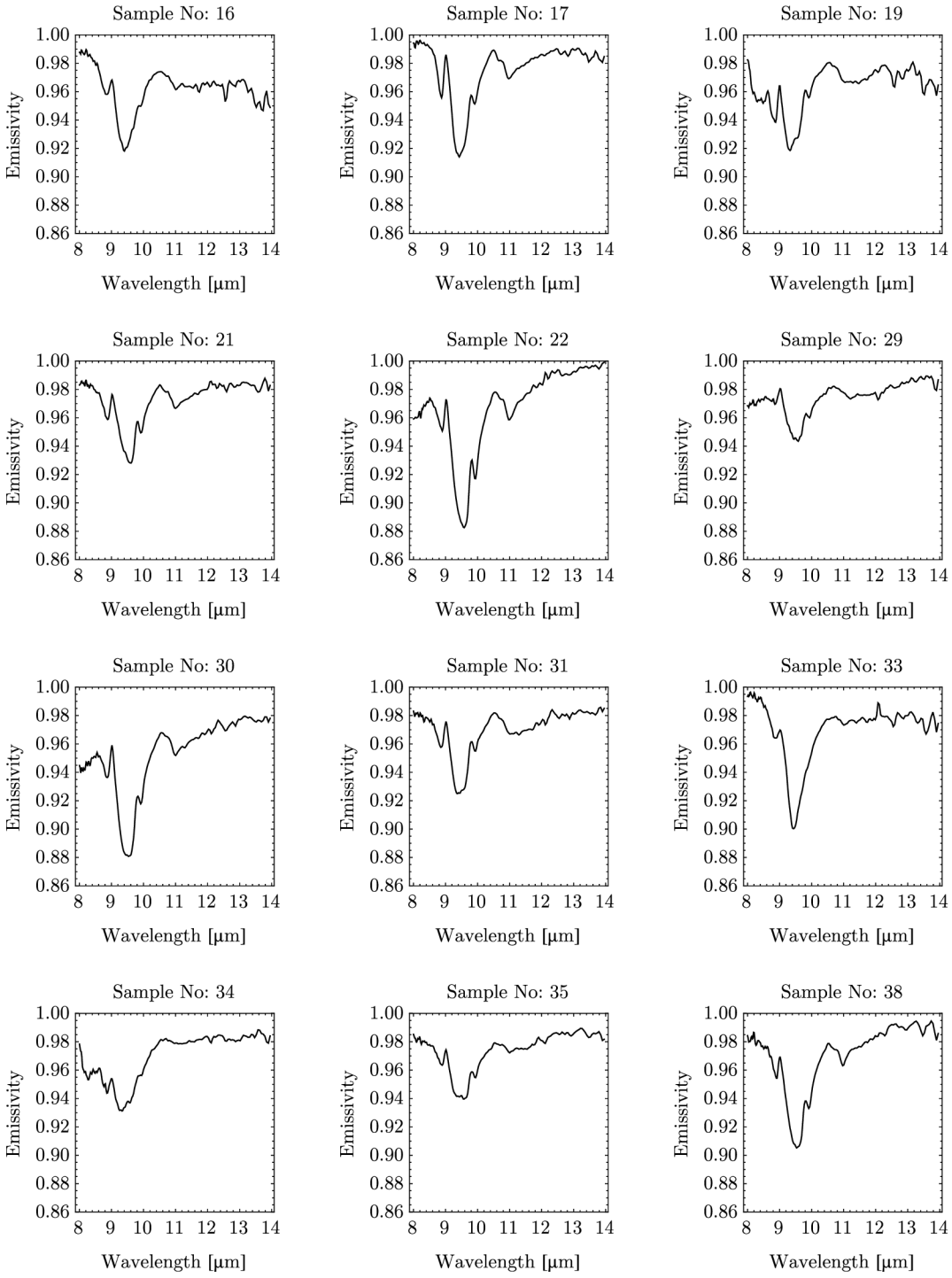

Figure A.5: Depiction of samples' emissivity spectra included in the library of spoil substrates.

B

Dependencies between city structure and thermal behaviour in Brno

Long lasting heat waves bring about more severe living conditions in large urban environments. The phenomenon has been addressed mainly as urban heat islands (UHI). Determination of factors affecting UHI and good understanding of dependencies between city structure and thermal behaviour can significantly help municipalities in long-term strategic decision-making. A complex research effort using remote sensing techniques has been performed in the 2015. This appendix summarizes the preliminary results of the research, which is discussed in depth in [3]. Let us note that TASI image data used for the OSTES testing in the Chapter 4 were acquired within the scope of this research activity.

B.1. Methods

The set of hyperspectral airborne data was collected in visible, near infrared, shortwave infrared and thermal infrared spectral regions using CASI, SASI and TASI sensors (Itres Ltd., Calgary, Canada), respectively. In addition to hyperspectral data, lidar mapping was performed using a Riegl 680i instrument (RIEGL, Austria). Taken together, these data have a high potential for providing valuable information relevant for modelling city thermal properties.

Data were acquired in both winter and summer days over the city of Brno, Czech Republic, both of which were climatologically extreme events. Winter acquisition was performed on 7th February 2015 at 21:53 (UTC). Summer acquisition was performed on 4th July 2015 at 14:03 (UTC) and at 20:59 (UTC). Complementary airborne laser scanning dataset was acquired on 22nd September 2015. The detailed description of data processing and study area is included in [3].

The Figures B.1 and B.2 present the dependencies between city structure and city thermal regime. All displayed quantities are self explanatory except absorbed energy. This quantity relates surface absorptivity and solar irradiation accumulated during the daylight hours of 4th July 2015. Surface absorptivity was computed by subtracting surface reflectance from one. Then the surface absorptivity was multiplied by the direct plus diffuse solar irradiation, which was computed by SAGA Lighting and Visibility module (SAGA, 2013). The resulting quantity is absorbed energy by the surface.

B.2. Results

Results of visualisation are presented in the Figure B.1 and the Figure B.2. Both figures have the following structure. The distance along the transect is represented by meters displayed on a horizontal axis. A true-colour composition from the CASI data is shown in the topmost panel. It contains yellow line indicating the transect along which were observed various quantities displayed in the following panels. Surface temperatures of a summer day and a summer night are shown in the second panel. Surface temperature of a winter night is shown in the third panel. A depiction of city structure is contained in the fourth panel. Digital terrain model (DTM) is shown in brown, while buildings are distinguished from high vegetation with grey and green colours, respectively. The NDVI is shown in the fifth panel and absorbed energy is shown in the last panel.

Several common observations can be made in both figures. The NDVI, as a measure of "greenness", follows a classification of high vegetation and also allows distinguishing between streets and a surfaces covered by grass. Local minima in absorbed energy follow shaded regions at the edges of buildings. Temperature over the areas covered by vegetation tends to be more stable and lower in average, while the temperature of streets and parking lots is significantly higher during summer day. We would like to point out several interesting features in the individual transects. These will be indicated by the distance in meters on the horizontal axis.

In Figure B.1 between 80 and 90 can be seen the stabilising role of vegetation – the temperature profile has a low variability as well as a lower average despite a higher amount of absorbed energy. In Figure B.1 at 305 and 390, two different roof surfaces can be observed – the rightmost one is dark, has a high absorptivity, while the leftmost one has a high reflectivity and reflects a cold sky in both summer and winter night. The region from 400 to 550 contains green areas which surrounds Špilberk castle. Summer day temperature is significantly lower in this region compared to other built up areas. The only notable temperature extreme is visible between 460 and 470 where the transect crosses a path walk.

The Figure B.2 shows interesting features as well. Roofs with high reflectivity can be observed at 160 – 170 and 530 – 540. The coldest places during a summer day are the river between 260 and 280 (which is on the other hand the warmest place in winter) and hard shadows next to high buildings, e.g. at 545. There is a notable shaded hillside between 40 and 50 causing temperature decrease in both summer day and night. There is an interesting dip in the summer night temperature profile between 360 and 370, which is presumably caused by a parked car in the parking lot. A dip in the summer temperature around 445 is caused by a roof window included in the transect.

B.3. Conclusion

The presented results show that hyperspectral image data with a high spatial resolution offers valuable information about the dependencies between the city structure and its thermal regime. Therefore the further analysis of these data should include quantification and modelling of various relations.

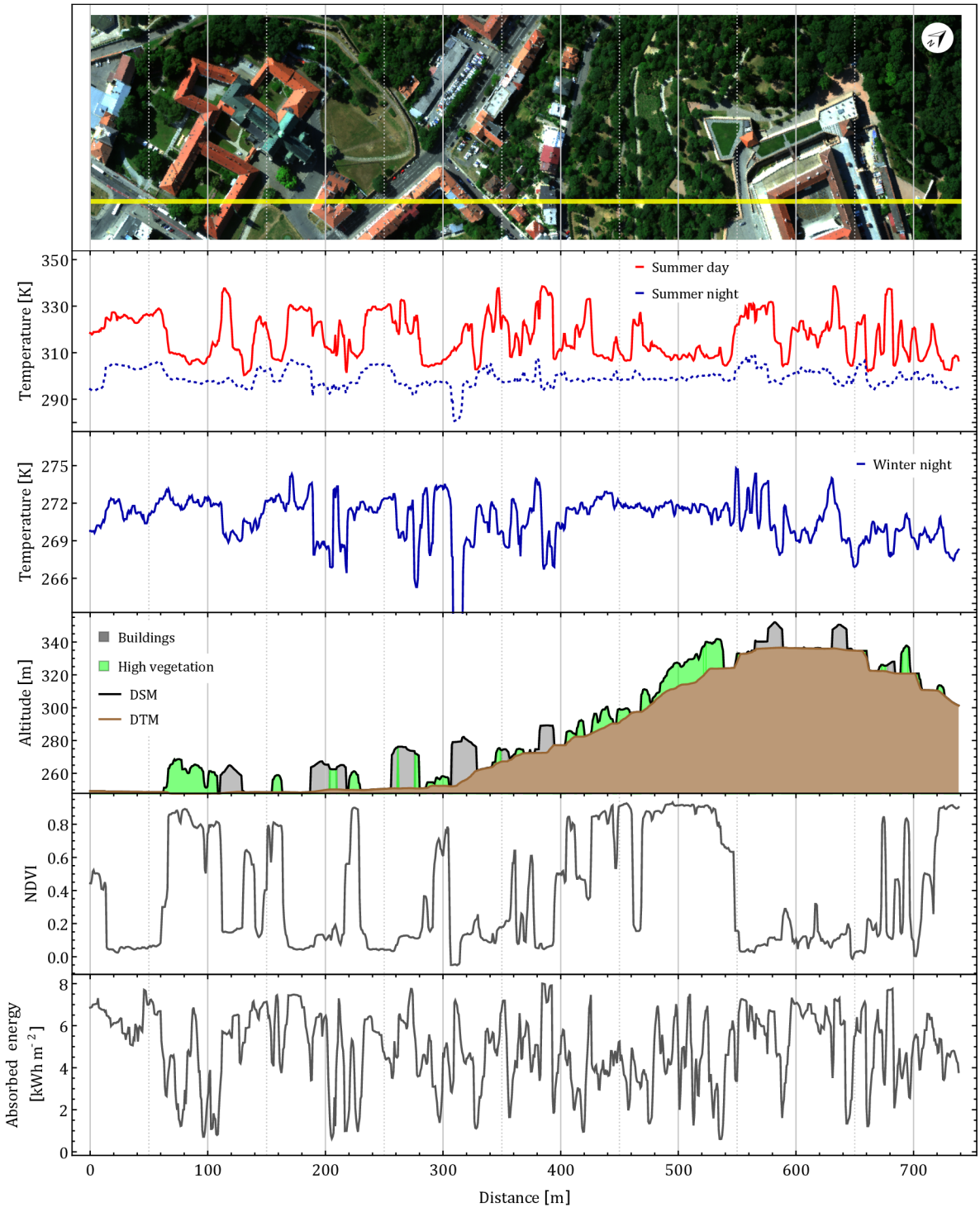

Figure B.1: Visualisation of various characteristics through the transect, which reveal various dependencies between city structure and thermal regime of the Brno city. Detailed description of the quantities and image data can be found in the text.

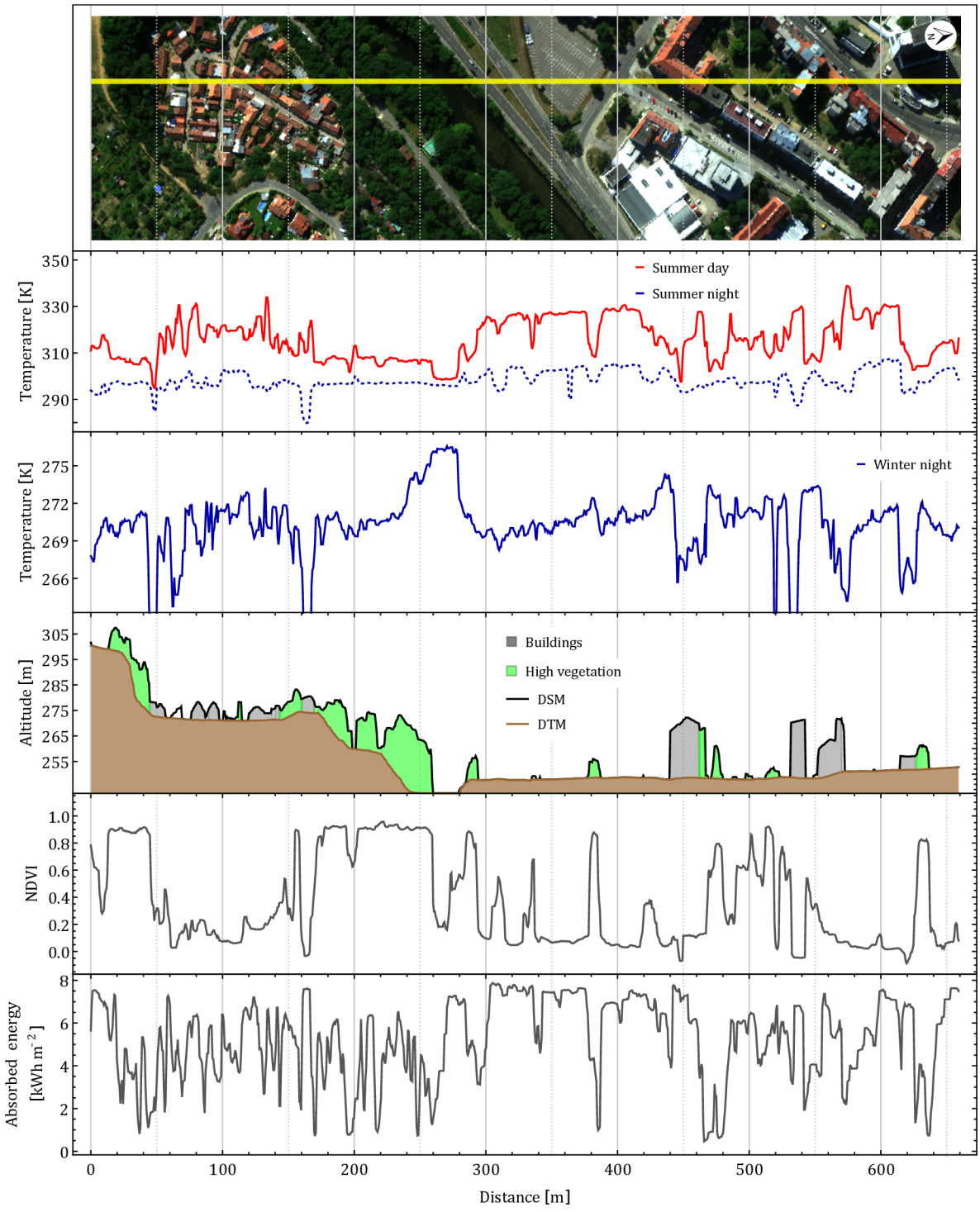

Figure B.2: Visualisation of various characteristics through the transect which reveal various dependencies between city structure and thermal regime of the Brno city. Detailed description of the quantities and image data can be found in the text.

Bibliography

Author's publications

[1] PIVOVARNÍK, M., KHALSA, S.J., JIMÉNEZ-MUÑOZ, J.C., ZEMEK, F. Improved Temperature and Emissivity Separation Algorithm for Multispectral and Hyperspectral Sensors. *IEEE Transactions on Geoscience and Remote Sensing*. DOI: 10.1109/TGRS.2016.2631508. (to be published)

[2] PIVOVARNÍK, M., PIKL, M., FROUZ, J., ZEMEK, F., KOPAČKOVÁ, V., NOTESCO, G. and BEN DOR, E. A Spectral Emissivity Library of Spoil Substrates. *Data*. 2016, **1**(12). DOI: 10.3390/data1020012

[3] NOVOTNÝ, J., PIVOVARNÍK, M., KHALSA, S.J. and ZEMEK, F. Visualisation of dependencies between city structure and thermal behaviour in Brno. **In:** *23rd International Archives of the Photogrammetry, Remote Sensing and Spatial Information Sciences Congress, ISPRS 2016*. Prague, 2016, 741-745. DOI: 10.5194/isprsarchives-XLI-B2-741-2016.

[4] JANOUTOVÁ, R., PIVOVARNÍK, M. Modelling of spruce trees using L-systems. **In:** *20th International Conference on Soft Computing: Evolutionary Computation, Genetic Programming, Swarm Intelligence, Fuzzy Logic, Neural Networks, Fractals, Bayesian Methods, MENDEL 2014*. Brno, 2014, 153-158. ISSN: 18033814.

Other references

[5] B. Eng, personal communication, 2015.

[6] BALDRIDGE, A.M., HOOK, S.J., GROVE, C.I. and RIVERA, G. The ASTER spectral library version 2.0. *Remote Sensing of Environment*. 2009, **113**(4), 711-715. DOI: 10.1016/j.rse.2008.11.007.

[7] BARDUCCI, A. and PIPPI, I. Temperature and emissivity retrieval from remotely sensed images using the "Grey body emissivity" method. *IEEE Transactions on Geoscience and Remote Sensing*. 1996, **34**(3), 681-695. DOI: 10.1109/36.499748.

[8] BERK, A., ANDERSON, G.P., ACHARYA, P.K., BERNSTEIN, L.S., MURATOV, L., LEE, J., FOX, M., ADLER-GOLDEN, S.M., CHETWYND, J.H., HOKE, JR. M.L., LOCKWOOD, R.B., GARDNER, J.A., COOLEY, T.W., BOREL, C.C., LEWIS, P.E. and SHETTLE, E.P. MODTRAN5: 2006 update. **In:** *Algorithms and Technologies for Multispectral, Hyperspectral, and Ultraspectral Imagery XII*. Orlando (Kissimmee), FL, 2006, F2331–F2331. DOI: 10.1117/12.665077.

[9] BORBAS, E., SEEMANN, S.W., KERN, A., MOY, L., LI, J., GUMLEY, L. and MENZEL, W.P. *MODIS Atmospheric Profile Retrieval - ATBD* [online]. 2011. [cit. 2016-08-10]. Available at: http://modis-atmos.gsfc.nasa.gov/_docs/MOD07_atbd_v7_April2011.pdf

[10] BOREL, C. Surface emissivity and temperature retrieval for a hyperspectral sensor. **In:** *IGARSS '98. Sensing and Managing the Environment. 1998 IEEE International Geoscience and Remote Sensing. Symposium Proceedings. (Cat. No.98CH36174).* Seattle, WA: IEEE, 1998, 546-549. DOI: 10.1109/IGARSS.1998.702966.

[11] BOREL, C. Error analysis for a temperature and emissivity retrieval algorithm for hyperspectral imaging data. *International Journal of Remote Sensing* [online]. 2008, **29**(17-18), 5029-5045. DOI: 10.1080/01431160802036540.

[12] BRADSHAW, A.D. and HÜTTL, R.F. Future minesite restoration involves a broader approach. Ecological Engineering. 2001, **17**(2-3), 87-90. DOI: 10.1016/S0925-8574(00)00149-X. ISSN 09258574.

[13] CHEVALLIER, F., CHÉRUY, F., SCOTT, N.A. and CHÉDIN, A. A neural network approach for a fast and accurate computation of a longwave radiative budget. *Journal of Applied Meteorology.* 1998, **37**(11), 1385-1397. DOI: 10.1175/1520-0450(1998)037¡1385:ANNAFA¿2.0.CO;2.

[14] CHÉDIN, A., SCOTT, N.A., WAHICHE, C. and MOULINIER, P. The improved initialization inversion method: a high resolution physical method for temperature retrievals from satellites of the TIROS-N series. *Journal of Climate and Applied Meteorology.* 1985, **24**(2), 128-143. DOI: 10.1175/1520-0450(1985)024¡0128:TIIIMA¿2.0.CO;2

[15] CHRISTENSEN, P.R., BANDFIELD, J.L., HAMILTON, V.E., HOWARD, D.A., LANE, M.D., PIATEK, J.L., RUFF, S.W. and STEFANOV, W.L. A thermal emission spectral library of rock-forming minerals. *Journal of Geophysical Research: Planets.* 2000, **105**(E4), 9735-9739. DOI: 10.1029/1998JE000624.

[16] CLARK, R.N., SWAYZE, G.A., WISE, R., LIVO, E., HOEFEN, T., KOKALY, R., SUTLEY, S.J. *USGS digital spectral library splib06a* [online]. U.S. Geological Survey, Digital Data Series 231, 2007. [cit. 2016-07-12]. Available at: http://speclab.cr.usgs.gov/spectral.lib06

[17] COLL, C., CASELLES, V., VALOR, E., NICLÒS, R., SÁNCHEZ, J.M., GALVE, J.M. and MIRA, M. Temperature and emissivity separation from ASTER data for low spectral contrast surfaces. *Remote Sensing of Environment.* 2007, **110**(2), 162-175. DOI: 10.1016/j.rse.2007.02.008.

[18] FERNÁNDEZ-RENAU, A., MEYNART, R., NEECK, S.P., GÓMEZ, J.A., DE MIGUEL, E. and SHIMODA, H. The INTA AHS system. **In:** *SPIE Proceedings.* Bruges: SPIE, 2005, 471-478. DOI: 10.1117/12.629440.

[19] FROUZ, J., KRIŠTŮFEK, V., BASTL, J., KALČÍK, J. and VAŇKOVÁ, H. Determination of Toxicity of Spoil Substrates After Brown Coal Mining Using a Laboratory

Reproduction Test with Enchytraeus crypticus (Oligochaeta). *Water, Air, & Soil Pollution*. 2005, **162**(1-4), 37-47. DOI: 10.1007/s11270-005-5991-y.

[20] FROUZ, J., LIVEČKOVÁ, M., ALBRECHTOVÁ, J., CHROŇÁKOVÁ, A., CAJTHAML, T., PIŽL, V., HÁNĚL, L., STARÝ, J., BALDRIAN, P., LHOTÁKOVÁ, Z., ŠIMÁČKOVÁ, H. and CEPÁKOVÁ, Š. Is the effect of trees on soil properties mediated by soil fauna? A case study from post-mining sites. *Forest Ecology and Management*. 2013, **309**, 87-95. DOI: 10.1016/j.foreco.2013.02.013.

[21] GARCIA-SANTOS, V., VALOR, E., CASELLES, V., MIRA, M., GALVE, J.M. a COLL, C. Evaluation of Different Methods to Retrieve the Hemispherical Downwelling Irradiance in the Thermal Infrared Region for Field Measurements. *IEEE Transactions on Geoscience and Remote Sensing*. 2013, **51**(4), 2155-2165. DOI: 10.1109/TGRS.2012.2209891.

[22] GILLESPIE, A.R., *Lithologic mapping of silicate rocks using TIMS* [online]. Jet Propulsion Lab., California Inst. of Tech., Pasadena, CA, United States, 1986. [cit. 2016-08-10]. Available at: http://ntrs.nasa.gov/search.jsp?R=19870007685

[23] GILLESPIE, A.R., ABBOTT, E.A., GILSON, L., HULLEY, G., JIMÉNEZ-MUÑOZ, J.C. and SOBRINO, J.A. Residual errors in ASTER temperature and emissivity standard products AST08 and AST05. *Remote Sensing of Environment*. 2011, **115**(12), 3681-3694. DOI: 10.1016/j.rse.2011.09.007.

[24] GILLESPIE, A.R., ROKUGAWA, S., HOOK, S., MATSUNAGA, T. and KAHLE, A.B. *Temperature/Emissivity Separation Algorithm Theoretical Basis Document, Version 2.4* [online]. Pasadena: Jet Propulsion Laboratory, 1999. [cit. 2016-01-19]. Available at: http://eospso.nasa.gov/sites/default/files/atbd/atbd-ast-05-08.pdf

[25] GILLESPIE, A.R., ROKUGAWA, S., MATSUNAGA, T., COTHERN, J.S., HOOK, S. and KAHLE, A.B. A temperature and emissivity separation algorithm for Advanced Spaceborne Thermal Emission and Reflection Radiometer (ASTER) images. *IEEE Transactions on Geoscience and Remote Sensing*. 1998, **36**(4), 1113-1126. DOI: 10.1109/36.700995.

[26] GU, D., GILLESPIE, A.R., KAHLE, A.B. and PALLUCONI, F.D. Autonomous atmospheric compensation (AAC) of high resolution hyperspectral thermal infrared remote-sensing imagery. *IEEE Transactions on Geoscience and Remote Sensing*. 2000, **38**(6), 2557-2570. DOI: 10.1109/36.885203.

[27] GUSTAFSON, W.T., GILLESPIE, A.R. and YAMADA, G.J. Revisions to the ASTER temperature/emissivity separation algorithm. **In:** *Second Recent Advances in Quantitative Remote Sensing*. Valencia, 2006, 770-775.

[28] HANUŠ, J., FABIÁNEK, T., KAPLAN, V. and HOMOLOVÁ, L. Flying laboratory of imaging systems (FLIS) at CzechGlobe. **In:** *SGEM2014 Conference Proceedings*. 2014, 177-182. DOI: 10.5593/SGEM2014/B23/S10.022. ISBN 978-619-7105-12-4. ISSN 1314-2704.

[29] HAMOUZ, K., LACHMAN, J., PIVEC, V. and ORSÁK, M. The effect of the conditions of cultivation on the content of polyphenol compounds in the potato varieties Agria and Karin. *Rostlinná Výroba*. 1997, **43**, 541-546.

[30] HOOK, S.J. and KAHLE, A.B. The micro fourier transform interferometer (uFTIR) — A new field spectrometer for acquisition of infrared data of natural surfaces. *Remote Sensing of Environment*. 1996, **56**(3), 172-181. DOI: 10.1016/0034-4257(95)00231-6.

[31] HORTON, K.A., JOHNSON, J.R. and LUCEY, P.G. Infrared Measurements of Pristine and Disturbed Soils 2. Environmental Effects and Field Data Reduction. Remote Sensing of Environment. 1998, **64**(1), 47-52. DOI: 10.1016/S0034-4257(97)00167-3.

[32] HOWELL, J.R. *Thermal radiation heat transfer*. 5th ed. Boca Raton: CRC Press, c2011. 957. ISBN 978-1-4398-0533-6.

[33] HULLEY, G. and HOOK, S.J. Generating Consistent Land Surface Temperature and Emissivity Products Between ASTER and MODIS Data for Earth Science Research. *IEEE Transactions on Geoscience and Remote Sensing*. 2011, **49**(4), 1304-1315. DOI: 10.1109/TGRS.2010.2063034.

[34] HULLEY, G. and HOOK, S.J. *HyspIRI Level-2 Thermal Infrared (TIR) Land Surface Temperature and Emissivity Algorithm Theoretical Basis Document* [online]. Pasadena, California: Jet Propulsion Laboratory, California Institute of Technology, 2011. [cit. 2016-01-19]. Available at: https://hyspiri.jpl.nasa.gov/downloads/Algorithm_Theoretical_Basis/HyspIRI_L2_Surface_Temperature_Emissivity_JPL_Pub_11-5_10102011.pdf

[35] ITRES. SparCal [software]. [access 1.3.2016]. Available at: http://www.itres.com/supporting-products/

[36] ITRES. RCX [software]. [access 1.3.2016]. Available at: http://www.itres.com/supporting-products/

[37] ITRES. GCSS [software]. [access 1.3.2016]. Available at: http://www.itres.com/supporting-products/

[38] JIMÉNEZ-MUÑOZ, J.C., CRISTOBAL, J., SOBRINO, J.A., SORIA, G., NINYEROLA, M. and PONS, X. Revision of the Single-Channel Algorithm for Land Surface Temperature Retrieval From Landsat Thermal-Infrared Data. *IEEE Transactions on Geoscience and Remote Sensing*. 2009, **47**(1), 339-349. DOI: 10.1109/TGRS.2008.2007125.

[39] JIMÉNEZ-MUÑOZ, J.C., SOBRINO, J.A. and GILLESPIE, A.R. Surface Emissivity Retrieval From Airborne Hyperspectral Scanner Data: Insights on Atmospheric Correction and Noise Removal. *IEEE Geoscience and Remote Sensing Letters*. 2012, **9**(2), 180-184. DOI: 10.1109/LGRS.2011.2163699.

[40] JIMÉNEZ-MUÑOZ, J.C., SOBRINO, J.A., MATTAR, C., HULLEY, G. and GOTTSCHE, F.-M. Temperature and Emissivity Separation From MSG/SEVIRI

Data. *IEEE Transactions on Geoscience and Remote Sensing*. 2014, **52**(9), 5937-5951. DOI: 10.1109/TGRS.2013.2293791.

[41] JONES, J.B. *Agronomic handbook: management of crops, soils, and their fertility*. Boca Raton, Fla.: CRC Press, c2003. ISBN 0849308976.

[42] KIRCHHOFF, G. Ueber das Verhältniss zwischen dem Emissionsvermögen und dem Absorptionsvermögen der Körper für Wärme und Licht. *Annalen der Physik und Chemie*. 1860, **185**(2), 275-301. DOI: 10.1002/andp.18601850205.

[43] KOTTHAUS, S., SMITH, T.E.L., WOOSTER, M.J. and GRIMMOND, C.S.B. Derivation of an urban materials spectral library through emittance and reflectance spectroscopy. *ISPRS Journal of Photogrammetry and Remote Sensing*. 2014, **94**, 194-212. DOI: 10.1016/j.isprsjprs.2014.05.005.

[44] LI, Z., TANG, B., WU, H., REN, H., YAN, G., WAN, Z., TRIGO, I.F. and SOBRINO, J.A. Satellite-derived land surface temperature: Current status and perspectives. *Remote Sensing of Environment* [online]. 2013, **131**, 14-37. DOI: 10.1016/j.rse.2012.12.008.

[45] MATSUNAGA, T. A Temperature-Emissivity Separation Method Using an Empirical Relationship between the Mean, the Maximum, and the Minimum of the Thermal Infrared Emissivity Spectrum. *Journal of the Remote Sensing Society of Japan*. 1994, **14**(3), 230–241. DOI: 10.11440/rssj1981.14.230

[46] MUSHKIN, A., BALICK, L.K., and GILLESPIE, A.R. Temperature/emissivity separation of MTI data using the Terra/ASTER TES algorithm. **In:** *Algorithms and Technologies for Multispectral, Hyperspectral, and Ultraspectral Imagery VIII*. Orlando, FL: SPIE, 2002, 328-337. DOI: 10.1117/12.478764.

[47] NOTESCO, G., KOPAČKOVÁ, V., ROJÍK, P., SCHWARTZ, G., LIVNE, I. and DOR, E. Mineral Classification of Land Surface Using Multispectral LWIR and Hyperspectral SWIR Remote-Sensing Data. A Case Study over the Sokolov Lignite Open-Pit Mines, the Czech Republic. *Remote Sensing*. 2014, **6**(8), 7005-7025. DOI: 10.3390/rs6087005.

[48] PASCUCCI, S., CASA, R., BELVISO, C., PALOMBO, A., PIGNATTI, S. and CASTALDI, F. Estimation of soil organic carbon from airborne hyperspectral thermal infrared data: a case study. *European Journal of Soil Science*. 2014, **65**(6), 865-875. DOI: 10.1111/ejss.12203.

[49] PIPIA, L., PEREZ, F., TARDA, A., MARTINEZ, L. and ARBIOL, R. Simultaneous usage of optic and thermal hyperspectral sensors for crop water stress characterization. **In:** *IEEE International Geoscience and Remote Sensing Symposium*. Munich: IEEE, 2012, 6661-6664. DOI: 10.1109/IGARSS.2012.6352071.

[50] PLANCK, M. Zur Theorie des Gesetzes der Energieverteilung im Normalspektrum. *Verhandlungen der Deutschen Physikalischen Gesellschaft*. 1900, **2**(17), p. 237-245.

[51] POGORZALA, D., MESSINGER, D., SALVAGGIO, C. and SCHOTT, J. Gas plume species identification in airborne LWIR imagery using constrained stepwise regression analyses. **In:** *Algorithms and Technologies for Multispectral, Hyperspectral, and Ultraspectral Imagery XI*, Orlando, FL: SPIE, 2005, 194–205, DOI:10.1117/12.603661.

[52] RIBEIRO DA LUZ, B. and CROWLEY, J.K. Identification of plant species by using high spatial and spectral resolution thermal infrared (8.0–13.5 µm) imagery. *Remote Sensing of Environment*. 2010, **114**(2), 404-413. DOI: 10.1016/j.rse.2009.09.019.

[53] RICHTER, R. a SCHLÄPFER, D. Geo-atmospheric processing of airborne imaging spectrometry data. Part 2: Atmospheric/topographic correction. *International Journal of Remote Sensing*. 2002, **23**(13), 2631-2649. DOI: 10.1080/01431160110115834.

[54] SABOL, Jr., D.E., GILLESPIE, A.R., ABBOTT, E. and YAMADA, G. Field validation of the ASTER Temperature–Emissivity Separation algorithm. *Remote Sensing of Environment*. 2009, **113**(11), 2328-2344. DOI: 10.1016/j.rse.2009.06.008.

[55] SALISBURY, J.W., WALTER, L.S., VERGO, N., D'ARIA, D.M. *Infrared (2.1-25 um) spectra of minerals*. Baltimore: John Hopkins University Press, 1991. ISBN 0801844398.

[56] SHUKLA, M. K. a R. LAL. Temporal Changes in Soil Organic Carbon Concentration and Stocks in Reclaimed Minesoils of Southeastern Ohio. *Soil Science*. 2005, **170**(12), 1013-1021. DOI: 10.1097/01.ss.0000187354.62481.91.

[57] SNYDER, W. C., WAN, Z., ZHANG, Y. and FENG, Y.-Z. Classification-based emissivity for land surface temperature measurement from space. *International Journal of Remote Sensing*. 1998, **19**(14), 2753-2774. DOI: 10.1080/014311698214497.

[58] SOBRINO, J.A., FRANCH, B., MATTAR, C., JIMÉNEZ-MUÑOZ, J.C. and CORBARI, C. A method to estimate soil moisture from Airborne Hyperspectral Scanner (AHS) and ASTER data: Application to SEN2FLEX and SEN3EXP campaigns. *Remote Sensing of Environment*. 2012, **117**, 415–428. DOI: 10.1016/j.rse.2011.10.018

[59] SOBRINO, J.A., JIMÉNEZ-MUÑOZ, J.C., BALICK, L., GILLESPIE, A.R., SABOL, D., and GUSTAFSON, W. Accuracy of ASTER Level-2 thermal-infrared Standard Products of an agricultural area in Spain. *Remote Sensing of Environment*. 2007, **106**(2), 146-153. DOI: 10.1016/j.rse.2006.08.010. ISSN 00344257.

[60] SOBRINO, J.A., JIMÉNEZ-MUÑOZ, J.C., LABED-NACHBRAND, J. and NERRY, F. Surface emissivity retrieval from Digital Airborne Imaging Spectrometer data. *Journal of Geophysical Research: Atmospheres*. 2002, **107**(D23). DOI: 10.1029/2002JD002197.

[61] SOBRINO, J.A., JIMÉNEZ-MUÑOZ, J.C., ZARCO-TEJADA, P.J., SEPULCRE-CANTÓ, G. and DE MIGUEL, E. Land surface temperature derived from airborne hyperspectral scanner thermal infrared data. *Remote Sensing of Environment*. 2006, **102**(1-2), 99-115. DOI: 10.1016/j.rse.2006.02.001.

[62] SOBRINO, J.A., MATTAR, C., PARDO, P., JIMÉNEZ-MUÑOZ, J.C., HOOK, S.J., BALDRIDGE, A. and IBAÑEZ, R. Soil emissivity and reflectance spectra measurements. *Applied Optics*. 2009, **48**(19), 3664-3670. DOI: 10.1364/AO.48.003664.

[63] SOBRINO, J.A., OLTRA-CARRIÓ, R., JIMÉNEZ-MUÑOZ, J.C., JULIEN, Y., SÒRIA, G., FRANCH, B. and MATTAR, C. Emissivity mapping over urban areas using a classification-based approach: Application to the Dual-use European Security IR Experiment (DESIREX). *International Journal of Applied Earth Observation and Geoinformation*. 2012, **18**, 141–147. DOI: 10.1016/j.jag.2012.01.022.

[64] SOBRINO, J.A. and RAISSOUNI, N. Toward remote sensing methods for land cover dynamic monitoring: Application to Morocco. *International Journal of Remote Sensing*. 2000, **21**(2), 353-366. DOI: 10.1080/014311600210876.

[65] SÒRIA, G. and J.A. SOBRINO. ENVISAT/AATSR derived land surface temperature over a heterogeneous region. *Remote Sensing of Environment*. 2007, **111**(4), 409-422. DOI: 10.1016/j.rse.2007.03.017.

[66] TONOOKA, H. Accurate atmospheric correction of ASTER thermal infrared imagery using the WVS method. *IEEE Transactions on Geoscience and Remote Sensing*. 2005, **43**(12), 2778-2792. DOI: 10.1109/TGRS.2005.857886.

[67] TONOOKA, H. and PALLUCONI, D. Verification of the ASTER/TIR atmospheric correction algorithm based on water surface emissivity retrieved. **In:** *Proceedings of the Society of Photo-optical Instrumentation Engineers*. San Diego, CA: SPIE, 2001, 51-58. DOI: 10.1117/12.455143.

[68] TONOOKA, H. and PALLUCONI, D. Validation of ASTER/TIR standard atmospheric correction using water surfaces. *IEEE Transactions on Geoscience and Remote Sensing*. 2005, **43**(12), 2769-2777. DOI: 10.1109/TGRS.2005.857883.

[69] TONOOKA, H., PALLUCONI, D., HOOK, S.J. and MATSUNAGA, T. Vicarious calibration of ASTER thermal infrared bands. *IEEE Transactions on Geoscience and Remote Sensing*. 2005, **43**(12), 2733-2746. DOI: 10.1109/TGRS.2005.857885.

[70] USSIRI, D.A.N., LAL, R. and JACINTHE, P.-A. Post-reclamation Land Use Effects on Properties and Carbon Sequestration in Minesoils of Southeastern Ohio. *Soil Science*. 2006, **171**(3), 261-271. DOI: 10.1097/01.ss.0000199702.68654.1e.

[71] Edited by VAN DER MEER, F.D. and DE JONG, S.M. *Imaging Spectrometry: Basic Principles and Prospective Applications*. Dordrecht: Kluwer Academic Publishers, 2001. ISBN 978-0-306-47578-8.

[72] VINDUŠKOVÁ, O. a FROUZ, J. Soil carbon accumulation after open-cast coal and oil shale mining in Northern Hemisphere: a quantitative review. *Environmental Earth Sciences*. 2013, **69**(5), 1685-1698. DOI: 10.1007/s12665-012-2004-5.

[73] WAN, Z. New refinements and validation of the MODIS Land-Surface Temperature/Emissivity products. *Remote Sensing of Environment*. 2008, **112**(1), 59-74. DOI: 10.1016/j.rse.2006.06.026.

[74] WANG, N., WU, H., NERRY, H., LI, C. and LI, Z. Temperature and Emissivity Retrievals From Hyperspectral Thermal Infrared Data Using Linear Spectral Emissivity Constraint. *IEEE Transactions on Geoscience and Remote Sensing*. 2011, **49**(4), 1291-1303. DOI: 10.1109/TGRS.2010.2062527.

[75] WANG, H., XIAO, Q., LI, H. and ZHONG, B. Temperature and emissivity separation algorithm for TASI airborne thermal hyperspectral data. **In:** *2011 International Conference on Electronics, Communications and Control (ICECC)*. Ningbo: IEEE, 2011, 1075-1078. DOI: 10.1109/icecc.2011.6066288.

[76] YOUNG, S.J. An in-scene method for atmospheric compensation of thermal hyperspectral data. *Journal of Geophysical Research*. 2002, **107**(D24). DOI: 10.1029/2001jd001266.

[77] Edited by ZEMEK, F.. *Airborne remote sensing: theory and practice in assessment of terrestrial ecosystems.* Brno: Global Change Research Institute CAS, 2014. 159. ISBN 978-80-87902-05-9.

List of used symbols and abbreviations

AAC	Autonomous atmospheric compensation
AHS	Airborne hyperspectral scanner
ARTEMISS	Automatic retrieval of temperature and emissivity using spectral smoothness
ASTER	Advanced spaceborne thermal emission and reflection radiometer
DAIS	Digital airborne imaging spectrometer
DEM/DTM	Digital elevation/terrain model
DN	Digital numbers
DSM	Digital surface model
EM	Electromagnetic
FTIR	Fourier transform infrared
FWHM	Full width at half maximum
ISAC	In-scene atmospheric corrections
LST	Land surface temperature
LSE	Land surface emissivity
LUT	Look-up tables
MMD	Maximum-minimum difference
MODIS	Moderate resolution imaging spectroradiometer
MODTRAN	MODerate resolution atmospheric TRANsmission model
MTI	Multispectral thermal imager
NDVI	Normalized difference vegetation index
NEΔT	Noise equivalent temperature difference
NEM	Normalization emissivity module
OSTES	Optimized smoothing for temperature emissivity separation
RTE	Radiative transfer equation
SEVIRI	Spinning enhanced visible and infrared imager
SLUM	Spectral library of urban materials
TASI	Thermal airborne spectrographic imager
TES	Temperature and emissivity separation algorithm
TIR	Thermal infrared
TIGR	TOVS initial guess retrieval
TUD	Atmospheric transmissivity, upwelling and downwelling atmospheric radiance